Whole-Process Modeling of Reservoir Turbidity Currents by a Double Layer-Averaged Model

Whole-process Modelling of Reservoir Turbidity Currents by a Double Layer-averaged Model

Zhixian Cao[1]; Ji Li[2]; Gareth Pender[3]; and Qingquan Liu[4]

[1] Professor, State Key Laboratory of Water Resources and Hydropower Engineering Science, Wuhan University, China; and Professor, Institute for Infrastructure and Environment, Heriot-Watt University, UK. E-mail: zxcao@whu.edu.cn

[2] PhD student, State Key Laboratory of Water Resources and Hydropower Engineering Science, Wuhan University, China. E-mail: lijimy0321@whu.edu.cn

[3] Professor, Institute for Infrastructure and Environment, Heriot-Watt University, UK; and Visiting Professor, State Key Laboratory of Water Resources and Hydropower Engineering Science, Wuhan University, China. Email: g.pender@hw.ac.uk

[4] Professor, Institute of Mechanics, Chinese Academy of Sciences, Beijing, China. Email: qqliu@imech.ac.cn

ABSTRACT

Turbidity current is formed as subaerial open-channel sediment-laden flow plunges into a reservoir. The whole process of reservoir turbidity current, i.e., formation, propagation and recession, is generally controlled by the water and sediment inputs from upstream and also the reservoir operation scheme specifying the downstream boundary condition. Enhanced understanding of reservoir turbidity current is critical to effective sediment management in alluvial rivers. However, until now there has been a lack of physically based and practically feasible models for resolving the whole process of reservoir turbidity current. This is because the computing cost of 3D modelling is excessively high. Also, single layer-averaged models cannot resolve the formation process characterized by the transition from open-channel sediment-laden flow to subaqueous turbidity current, or the upper clear-water flow as dictated by the operation scheme of the reservoir, which has significant impacts on turbidity current. Here a new 2D double layer-averaged model is proposed to facilitate for the first time whole-process modelling of reservoir turbidity current. The two hyperbolic systems of the governing equations for the two layers are solved separately and synchronously. The model is well balanced as the inter-layer interactions are negligible compared to inertia and gravitation, featuring a reasonable balance between the flux gradients and the bed or interface slope source terms and thus applicable to irregular topographies. The model is benchmarked against a spectrum of experimental cases, including turbidity currents due to lock-exchange and sustained inflow. It is revealed that an appropriate clear-water outflow is favourable for turbidity current propagation and conducive to improving sediment flushing efficiency. This is significant for optimizing reservoir operation schemes. As applied to turbidity current in the Xiaolangdi Reservoir in the Yellow River, China, the model successfully resolves the whole process from formation to recession. The present work facilitates a viable and promising framework for whole process modelling of turbidity currents, in support of reservoir sediment management.

Keywords: *Reservoir; turbidity current; sedimentation; sediment flushing; double layer-averaged model; reservoir management*

INTRODUCTION

Reservoir turbidity current is subaqueous, sediment-laden underflow. It is formed when subaerial, open-channel sediment-laden flow plunges into a reservoir. Like other gravity currents, it is driven by the density difference from the ambient fluid. More importantly, the whole process of reservoir turbidity current, i.e., formation, propagation and recession, is generally controlled by the water and sediment inputs from upstream and also the reservoir operational scheme specifying the downstream boundary condition. In this sense, reservoir turbidity currents are distinct from self-accelerating turbidity currents in ocean environments (Parker et al. 1986). In general, turbidity currents can travel remarkable distances carrying large amounts of suspended sediment from the plunge point to the downstream. In reservoirs, turbidity currents are often the governing processes for the transport, entrainment and deposition of sediment (Fan and Morris 1992a). If the turbidity currents can manage to arrive at the dam, it will be possible to flush sediment out of the reservoir. Otherwise, severe sedimentation in the reservoir will generally occur. Enhanced understanding of the whole process of reservoir turbidity currents is critical to effective sediment and reservoir management.

Previous studies have focused on the threshold condition for the formation of turbidity current based on the densimetric Froude number at the plunge point, derived from laboratory experiments (Fan 1960; Singh and Shah 1971) or analytical models (Savage and Brimberg 1975; Akiyama and Stefan 1984; Parker and Toniolo 2007; Dai and Garcia 2009; Li et al. 2011). However, these cannot provide enough and effective information to quantify the whole process of reservoir turbidity currents. Also, laboratory experiments have been used to investigate the evolutional characteristics of turbidity currents (Hürzeler et al. 1996; Lee and Yu 1997; Gladstone et al. 1998; Hallworth and Huppert 1998) and the vertical structure of the currents (Altinakar et al. 1996; Eggenhuisen and McCaffrey 2011; Nourmohammadi et al. 2011). Especially, Lee and Yu (1997) performed a series of tests to investigate the formation and propagation of turbidity currents due to sustained inflow and in particular demonstrated the impacts of various upstream and downstream boundary conditions. Also, they investigated the densimetric Froude number at both the incipient and stable plunge points. Yet flume experiments are constrained by the relatively small spatial scales. Interestingly, a series of large field-scale water-sediment regulation experiments has been undertaken by the Yellow River Water

78 Resources Commission (YRCC 2007) since 2002. Turbidity currents were formed in the Xiaolangdi
79 Reservoir by plunging of the sediment-laden floods released from the Sanmenxia Reservoir at the
80 upstream and believed to be the most important means for sediment flushing. A significant volume of
81 hydrological data was collected, concerning the location of the front, average velocity and sediment
82 concentration of the turbidity currents. The field experiments are certainly essential in support of not
83 only practical sediment management, but also development and applications of analytical and
84 computational models.

85 Computational modelling is certainly attractive, as detailed processes of reservoir turbidity
86 currents can be resolved. Generally, there have been two categories of computational models for
87 turbidity currents, i.e., depth-resolving models and layer-averaged models. Depth-resolving models,
88 including 3D and vertical 2D models, can reproduce the evolution process and the vertical structure of
89 turbidity currents (e.g., Bournet et al. 1999; De Cesare et al. 2001; Kassem and Imran 2001; Kassem et
90 al. 2003; Khan et al. 2005; Huang et al. 2007, 2008; Georgoulas et al. 2010; An and Julien 2014). And
91 indeed, there have been modelling efforts to resolve the formation of turbidity currents (Kassem and
92 Imran 2001; De Cesare et al. 2001; Georgoulas et al. 2010). Nevertheless, depth-resolving models
93 require excessively high computational costs and thus are unrealistic for applications to large-scale
94 proto-type turbidity currents such as those in the Xiaolangdi Reservoir, Yellow River in China. This
95 holds true for general 3D models for fluvial flow and sediment transport (Fang and Wang 2000; Wu et
96 al. 2000). Also, the physics of turbulent turbidity currents, on which the model closures are based, is
97 still poorly understood. In particular, it remains far from clear how to incorporate the effects of
98 sediment into turbulence closures, even for steady and uniform sediment-laden flows in open channels.
99 Comparatively, layer-averaged models are easier to formulate and solve. Layer-averaged refers to the
100 fact that the physical quantities (velocity and sediment concentration) are averaged along the thickness
101 of the turbidity currents. However, to date, most existing layer-averaged models for turbidity currents
102 are single layer-averaged models, in which the upper clear-water flow is ignored and not modelled at
103 all (e.g., Fukushima et al. 1985; Parker et al. 1986; Choi 1998; Bradford and Katopodes 1999a, b;
104 Sequeiros et al. 2009; Hu et al. 2012; Lai and Wu 2013). Thus they are restricted to modelling the
105 propagation of turbidity currents after their formation. In applications, this category of models hinges
106 upon observed data to specify the upstream boundary conditions (e.g., Hu et al. 2012), which however

is not generally available. Critically, single layer-averaged models cannot resolve the formation process characterized by the transition from subaerial open-channel sediment-laden flow to subaqueous turbidity current, or the upper clear-water flow dictated by the operation scheme of the reservoir. In contrast to these limitations, it is fundamental to resolve the formation process of reservoir turbidity current, not only scientifically but also practically. Equally importantly the operation scheme of the reservoir has been found to have significant impacts on turbidity currents (Lee and Yu 1997). Until now there have been no layer-averaged models capable of modelling the whole process of reservoir turbidity currents, which is critical to effective sediment and reservoir management. In this connection, double layer-averaged models have been developed for general gravity currents (Rottman and Simpson 1983; Bonnecaze et al. 1993; Hallworth et al. 2003; Ungarish and Zemach 2005; Adduce et al. 2012; La Rocca et al. 2012). Two sets of layer-averaged equations are deployed to describe respectively the gravity current layer and the upper clear-water flow layer. It is also noted that Dallimore et al. (2004) has employed a coupled 3D hydrodynamics and 2D layer-averaged model to simulate the formation and subsequent propagation process of reservoir saline underflows. However, most existing double layer-averaged models have not incorporated sediment transport and morphological evolution, which however are key features of reservoir turbidity currents over mobile bed. The 1D double layer-averaged model by Bonnecaze et al. (1993) takes into account sediment deposition, but ignores bed sediment entrainment and morphological evolution. Also it is limited to lock-exchange gravity currents without inflow from the upstream or outflow at the downstream boundary. Strictly, the lock-exchange gravity current is not reservoir turbidity current that is normally dictated by the water and sediment inputs from the upstream and outflow at the downstream.

A new 2D well-balanced double layer-averaged model is developed here to facilitate for the first time whole process modelling of reservoir turbidity currents. The model is extended from the recent 1D non well-balanced double layer-averaged model (Li et al. 2013). The two hyperbolic systems of the governing equations for the two layers are solved separately and synchronously. Each hyperbolic system is solved by a quasi-well-balanced numerical algorithm involving drying and wetting, using a second-order accurate Godunov-type finite volume method in conjunction with the HLLC (Harten-Lax-van Leer Contact Wave) approximate Riemann solver. The model is benchmarked

against a spectrum of experimental turbidity currents induced by lock-exchange (Bonnecaze et al. 1995) and sustained inflow (Lee and Yu 1997). A pilot study is presented of large-scale proto-type turbidity current in the Xiaolangdi Reservoir (Li 2004; YRCC 2007), Yellow River in China to demonstrate the capability of the present model.

MATHEMATICAL MODEL

Governing Equations

In general, there exist interactions among the upper layer clear water flow, turbidity current and the erodible bed, which are characterized by mass and momentum exchanges. Coupled modelling is generally justified, which has been implemented in recent single layer-averaged models (Hu and Cao 2009; Hu et al. 2012). This is followed in the present 2D double layer-averaged model. The governing equations of the model are essentially 2D shallow water equations comprising the mass and momentum conservation equations respectively for the clear-water flow layer and the turbidity current layer, and also the mass conservation equations for sediment in the turbidity current layer and bed sediment respectively. By analogy to 1D case (Li et al. 2013), these are

$$\frac{\partial \mathbf{T}}{\partial t}+\frac{\partial \mathbf{E}}{\partial x}+\frac{\partial \mathbf{F}}{\partial y}=\mathbf{R}_b+\mathbf{R}_f+\mathbf{R}_e \tag{1}$$

$$\frac{\partial \mathbf{U}}{\partial t}+\frac{\partial \mathbf{G}}{\partial x}+\frac{\partial \mathbf{H}}{\partial y}=\mathbf{S}_b+\mathbf{S}_f+\mathbf{S}_e \tag{2}$$

$$\mathbf{T}==\begin{bmatrix}\eta\\ q_{wx}\\ q_{wy}\end{bmatrix}=\begin{bmatrix}\eta\\ h_w u_w\\ h_w v_w\end{bmatrix},\quad \mathbf{E}=\begin{bmatrix}h_w u_w\\ h_w u_w^2+0.5g\left(\eta^2-2\eta\eta_s\right)\\ h_w u_w v_w\end{bmatrix},\quad \mathbf{F}=\begin{bmatrix}h_w v_w\\ h_w u_w v_w\\ h_w v_w^2+0.5g\left(\eta^2-2\eta\eta_s\right)\end{bmatrix} \tag{3a, b, c}$$

$$\mathbf{R}_b=\begin{bmatrix}0\\ -g\eta\dfrac{\partial \eta_s}{\partial x}\\ -g\eta\dfrac{\partial \eta_s}{\partial y}\end{bmatrix},\quad \mathbf{R}_f=\begin{bmatrix}0\\ -\dfrac{\tau_{wx}}{\rho_w}-E_w u_w\\ -\dfrac{\tau_{wy}}{\rho_w}-E_w v_w\end{bmatrix},\quad \mathbf{R}_e=\begin{bmatrix}-E_w+\dfrac{\partial \eta_s}{\partial t}\\ 0\\ 0\end{bmatrix} \tag{3d, e, f}$$

155 $$\mathbf{U}=\begin{bmatrix}\eta_s\\ q_{sx}\\ q_{sy}\\ q_c\end{bmatrix}=\begin{bmatrix}\eta_s\\ h_s u_s\\ h_s v_s\\ h_s c_s\end{bmatrix},\ \mathbf{G}=\begin{bmatrix}h_s u_s\\ h_s u_s^2+0.5g\left(\eta_s^2-2\eta_s z_b\right)\\ h_s u_s v_s\\ h_s u_s c_s\end{bmatrix},\ \mathbf{H}=\begin{bmatrix}h_s v_s\\ h_s u_s v_s\\ h_s u_s^2+0.5g\left(\eta_s^2-2\eta_s z_b\right)\\ h_s v_s c_s\end{bmatrix} \quad (4a, b, c)$$

156 $$\mathbf{S}_b=\begin{bmatrix}0\\ -g\eta_s\dfrac{\partial z_b}{\partial x}\\ -g\eta_s\dfrac{\partial z_b}{\partial y}\\ 0\end{bmatrix},\ \mathbf{S}_f=\begin{bmatrix}0\\ N_x\\ N_y\\ E-D\end{bmatrix},\ \mathbf{S}_e=\begin{bmatrix}E_w\\ 0\\ 0\\ 0\end{bmatrix} \quad (4d, e, f)$$

157 $$N_x=\frac{\tau_{wx}-\tau_{bx}}{\rho_c}-\frac{\rho_w g}{\rho_c}h_s\frac{\partial h_w}{\partial x}-\frac{\left(\rho_0-\rho_c\right)\left(E-D\right)u_s}{\left(1-p\right)\rho_c}+\frac{\left(\rho_s-\rho_w\right)c_s u_s E_w}{\rho_c}+\frac{\rho_w E_w u_w}{\rho_c}-\frac{\left(\rho_s-\rho_w\right)g h_s^2}{2\rho_c}\frac{\partial c_s}{\partial x} \quad (4g)$$

158 $$N_y=\frac{\tau_{wy}-\tau_{by}}{\rho_c}-\frac{\rho_w g}{\rho_c}h_s\frac{\partial h_w}{\partial y}-\frac{\left(\rho_0-\rho_c\right)\left(E-D\right)v_s}{\left(1-p\right)\rho_c}+\frac{\left(\rho_s-\rho_w\right)c_s v_s E_w}{\rho_c}+\frac{\rho_w E_w v_w}{\rho_c}-\frac{\left(\rho_s-\rho_w\right)g h_s^2}{2\rho_c}\frac{\partial c_s}{\partial y} \quad (4h)$$

159 $$\frac{\partial z_b}{\partial t}=-\frac{E-D}{1-p} \quad (5)$$

160 where $\mathbf{T}$ and $\mathbf{U}$ are the conserved variables; $\mathbf{E}$, $\mathbf{F}$, $\mathbf{G}$ and $\mathbf{H}$ are the flux variables. For the
161 turbidity current layer, $\mathbf{S}_b$ denotes bed slope source term, $\mathbf{S}_f$ includes bed friction source terms
162 and other terms related to the impacts of sediment transport and water entrainment, $\mathbf{S}_e$ represents
163 water entrainment source term. Similarly, for the clear-water flow layer, $\mathbf{R}_b$ features interface slope
164 source term, $\mathbf{R}_f$ comprises interface friction source terms and other terms related to impacts of
165 water entrainment, $\mathbf{R}_e$ represents water entrainment source term and variations of interface elevation;
166 q_{wx}, q_{wy} are conservative variables in Eq. (3); q_{sx}, q_{sy}, q_c conservative variables in Eq. (4); t
167 is the time; g the gravitational acceleration; x, y are the horizontal coordinates; η is the water
168 surface elevation; η_s the elevation of interface between the clear-water layer and turbidity current

layer; h_w the depth of clear-water layer; u_w, v_w are the layer-averaged velocities of clear-water layer in the x- and y- directions; h_s is the depth of turbidity current layer; u_s, v_s are the layer-averaged velocities of turbidity current layer in the x- and y- directions; c_s is the layer-averaged volumetric sediment concentration of the turbidity current layer; z_b bed elevation; p the bed sediment porosity; ρ_w, ρ_s are the densities of water and sediment respectively; $\rho_c = \rho_w(1-c_s) + \rho_s c_s$ is the density of the water-sediment mixture in the turbidity current layer; $\rho_0 = \rho_w p + \rho_s(1-p)$ the density of the saturated bed; E and D are the sediment entrainment and deposition fluxes across the bottom boundary respectively; τ_{wx}, τ_{wy} are the shear stresses at the interface between the clear-water flow layer and the turbidity current layer in the x- and y- directions; and τ_{bx}, τ_{by} are bed shear stresses in the x- and y- directions; E_w is the mass flux of water entrainment across the interface between the two layers.

Model Closure

To close the governing equations of the present 2D double layer-averaged model, a set of relationships has to be introduced to determine the boundary resistance, interface shear stress and water entrainment and sediment exchange fluxes. Generally, unsteady and non-uniform flows may experience boundary resistances substantially different from those of steady and uniform flows. This is more pronounced when sediment transport is involved, which renders the bed movable and bedforms generated. However, no generally applicable relationships are currently available to represent boundary resistance in such flows. This is also the case for the interface shear stress, for which there has been different empirical relationships (Chen and Peng 2006; Kim and LeVeque 2008; Zech et al. 2008; Lee et al. 2014). Consequently, computational studies of turbidity currents over fixed and mobile beds continue to use resistance relationships initially developed for steady and uniform flows, which are usually based on the Manning's equation. This practice is followed for the present 2D double layer-averaged model by virtue of the conventional empirical relations

194 $$\tau_{wx} = \rho_w g n_w^2 (u_w - u_s)\overline{U}_{ws} / h_w^{1/3}, \quad \tau_{wy} = \rho_w g n_w^2 (v_w - v_s)\overline{U}_{ws} / h_w^{1/3} \tag{6a, b}$$

195 $$\tau_{bx} = \rho_c g n_b^2 u_s \overline{U}_s / h_s^{1/3}, \quad \tau_{bx} = \rho_c g n_b^2 v_s \overline{U}_s / h_s^{1/3} \tag{7a, b}$$

196 where n_w is the roughness at the interface between the turbidity current layer and clear-water flow
197 layer; n_b the roughness of the bed; $\overline{U}_s = \sqrt{u_s^2 + v_s^2}$, the resultant velocity of the turbidity current
198 layer; and $\overline{U}_{ws} = \sqrt{(u_w - u_s)^2 + (v_w - v_s)^2}$, the resultant velocity difference between the two layers.

199 The mass flux of water entrainment E_w represents the mixing of the turbidity current with the
200 clear water across the interface of two layers. It is determined by (Parker et al. 1986)

201 $$E_w = e_w \overline{U}_{ws} \tag{8}$$

202 where the water entrainment coefficient e_w is calculated empirically using the Richardson number
203 $\mathrm{Ri} = g' h_s / \overline{U}_{ws}^2$ and the submerged gravitational acceleration $g' = sgc_s$ with specific gravity of
204 sediment $s = \rho_s / \rho_w - 1$,

205 $$e_w = \frac{0.00153}{0.0204 + \mathrm{Ri}} \tag{9}$$

206 The sediment deposition flux can be approximated by the product of the local near-bed sediment
207 concentration and the sediment settling velocity. Sediment entrainment is assumed to occur at the
208 same rate as it does under capacity conditions. Thus

209 $$E = \omega E_s, \quad D = \omega c_b \tag{10a, b}$$

210 where ω is the settling velocity of a single sediment particle in tranquil clear water, calculated using
211 Zhang's formula (Zhang and Xie 1993); $c_b = r_b c_s$ the local near-bed concentration, r_b can be
212 determined by (Parker et al. 1986)

213 $$r_b = 1 + 31.5(\sqrt{u_*^2 + v_*^2} / \omega)^{-1.46} \tag{11}$$

where u_* and v_* are the bed shear velocities in the x- and y- directions. The parameter E_s is the near-bed concentration at capacity condition. Parker et al. (1986) proposed the following empirical formulation,

$$E_s = \begin{cases} 0.3 & \psi \geq 13.2 \\ 3\times 10^{-12}\psi^{10}(1-5\psi^{-1}) & 5.0 < \psi < 13.2 \\ 0 & \psi \leq 5.0 \end{cases} \tag{12}$$

where $\psi = \sqrt{(u_*^2 + v_*^2)\sqrt{sgd^3}/\nu}/\omega$, d is medium sediment particle diameter, and ν is kinematic viscosity of water. In the present study, the Zhang and Xie formula is also adopted, which is well tested and widely used for suspended sediment transport of open channel flow in the Yellow River (Zhang and Xie 1993). A correction coefficient α is introduced because the present study is concerned with turbidity currents. Following the logarithmic-matching treatment of Guo (2002), the Zhang and Xie formula reads

$$E_s = \alpha \frac{1}{20\rho_s} \frac{\left(\overline{U}_s^3/gh_s\omega\right)^{1.5}}{1+\left(\overline{U}_s^3/45gh_s\omega\right)^{1.15}} \tag{13}$$

Numerical Algorithm

Although there have been analyses of double layer-averaged models over fixed beds regarding hyperbolicity and Kelvin-Helmholtz instability, Eqs. (1) to (5) constitute a nonlinear system of eight partial differential equations, involving more equations than previously analyzed (e.g., Kim and LeVeque 2008; Castro et al. 2010). It is too complicated to be solved numerically as a single system presently, which is reserved for future studies. Therefore an alternative solution strategy is proposed. As bed deformation is entirely determined by local entrainment and deposition fluxes under the non-capacity framework for sediment transport, Eq. (5) is separated from the remaining equations and can be readily solved. Also, from physical considerations, either the clear-water flow layer or the turbidity current layer is mainly dictated by its own inertia, gravity and boundary resistance, whilst the inter-layer interactions [mainly the second terms on the right hand side of Eq. 4 (g and h)] play a secondary role and can therefore be set as source terms in the momentum equations. In fact, the

inter-layer interactions can be confirmed to be negligible *post priori*, after the numerical solution of a specific case has been achieved.

Given the observations above, the two non-homogeneous hyperbolic systems constituted by Eqs. (1) and (2) can be solved separately and synchronously (Li et al. 2013) using one of a hierarchy of numerical algorithms that can capture shock waves and contact discontinuities properly. The numerical algorithm employed in the present double layer-averaged mobile model is an extension of that in the 2D model originally developed for single-layer clear-water flow over fixed bed (Liang 2010). Take Eq. (2) as an example. It can be solved numerically by an accurate finite volume Godunov-type approach in conjunction with the HLLC (Harten-Lax-van Leer contact wave) approximate Riemann solver (Toro 2001) on a fixed rectangular mesh. In principle, the present model is well-balanced as the inter-layer interactions play secondary roles and are negligible compared to inertia and gravitation.

The following time-marching formulas are used to update flow and sediment variables to a new time step ($k+1$)

$$\mathbf{U}_{i,j}^{q} = \mathbf{U}_{i,j}^{k} + \Delta t \mathbf{S}_{f\,i,j}^{k+1} \tag{14}$$

$$\mathbf{U}_{i,j}^{k+1} = \mathbf{U}_{i,j}^{r} - \frac{\Delta t(\mathbf{G}_{i+1/2,j} - \mathbf{G}_{i-1/2,j})^{q}}{\Delta x} - \frac{\Delta t(\mathbf{H}_{i,j+1/2} - \mathbf{H}_{i,j-1/2})^{q}}{\Delta y} + \Delta t \mathbf{S}_{b\,i,j}^{k} + \Delta t \mathbf{S}_{e\,i,j}^{k} \tag{15}$$

where the subscript k represents the time level and q indicates the state after calculating the variables from Eq. (14); subscripts i, j are the spatial node indexes; Δt is the time step; Δx, Δy are the spatial steps; $\mathbf{G}_{i+1/2,j}$, $\mathbf{G}_{i-1/2,j}$, $\mathbf{H}_{i+1/2,j}$ and $\mathbf{H}_{i-1/2,j}$ the interface fluxes.

In Eq. (14), the friction source term $\mathbf{S}_{f}^{k+1}$ is solved by a splitting method; it is equivalent to solving the ordinary differential equations

$$\frac{d\mathbf{U}}{dt} = \mathbf{S}_{f} \tag{16}$$

Consider the momentum equation of Eq. (16) in the x - direction

$$\frac{dq_{sx}}{dt} = \mathbf{S}_{fx} = N_x \tag{17}$$

Eq. (17) is then discretised by a full implicit method

$$\frac{q_{sx}^{q} - q_{sx}^{k}}{\Delta t} = \mathbf{S}_{fx}^{k+1} \tag{18}$$

where the friction term is expressed using a Taylor series as

$$\mathbf{S}_{fx}^{k+1} = \mathbf{S}_{fx}^{k} + \left(\partial \mathbf{S}_{fx} / \partial q_{sx}\right)^{k} \Delta q_{sx} + \mathrm{O}\left(\Delta q_{sx}^{2}\right) \tag{19}$$

where $\Delta q_{sx} = q_{sx}^{q} - q_{sx}^{k}$. Neglecting the high-order terms and substituting it into Eq. (18), the following formula is attained for updating q_{sx} to the q time step

$$q_{sx}^{q} = q_{sx}^{k} + \Delta t\left(\mathbf{S}_{fx} / D_x\right)^{k} = q_{sx}^{k} + \Delta t F_x \tag{20}$$

where $D_x = 1 - \Delta t\left(\partial \mathbf{S}_{fx} / \partial q_{sx}\right)^{k}$ is the implicit coefficient and $F_x = \mathbf{S}_{fx} / D_x$ is the friction source term including the implicit coefficient. In order to ensure stability, a limiting value of the implicit friction force must be identified according to the physics of the shallow flows. The maximum effect of the friction force is to constrain the flow (i.e. $q_{sx}^{q} q_{sx}^{k} \geq 0$). Then, according to Eq. (20), the limiting value of the implicit friction force can be easily derived as

$$F_x = \begin{cases} \geq -q_{sx}^{k} / \Delta t & if\ q_{sx}^{k} \geq 0 \\ \leq -q_{sx}^{k} / \Delta t & if\ q_{sx}^{k} \leq 0 \end{cases} \tag{21}$$

If F_x is computed beyond the limit, its value is replaced by the critical value $F_x = -q_{sx}^{k} / \Delta t$ in the actual computation. Similarly, the implicit coefficient in the y - direction can be calculated. In Eq. (17), the terms $\partial c_s / \partial x$ and $\partial h_w / \partial x$ are discretised using a central difference scheme for simplicity.

When evaluating $\mathbf{U}_{i,j}^{k+1}$ in Eq. (15), the solution of Eq. (14) is used as the initial condition. The interface fluxes $\mathbf{G}_{i+1/2,j}$, $\mathbf{G}_{i-1/2,j}$, $\mathbf{H}_{i+1/2,j}$ and $\mathbf{H}_{i-1/2,j}$ are computed using the HLLC Riemann solver (Toro 2001), which needs correct reconstruction of the Riemann states. The MUSCL method is

used to achieve second-order accuracy in space. The Riemann states are defined by using the minmod slope-limited reconstruction. At the left hand side of the cell interface $(i+1/2, j)$, the values are evaluated by

$$\overline{\eta}^{L}_{i+1/2,j} = \eta_{i,j} + 0.5\varphi(\eta_{i,j} - \eta_{i-1,j}),\ \ \overline{h}^{L}_{s\,i+1/2,j} = h_{s\,i,j} + 0.5\varphi(h_{s\,i,j} - h_{s\,i-1,j}) \tag{22a, b}$$

$$\overline{z}^{L}_{b\,i+1/2,j} = z_{b\,i,j} + 0.5\varphi(z_{b\,i,j} - z_{b\,i-1,j}),\ \ \overline{q}^{L}_{sx\,i+1/2,j} = q_{sx\,i,j} + 0.5\varphi(q_{sx\,i,j} - q_{sx\,i-1,j}) \tag{22c, d}$$

$$\overline{q}^{L}_{sy\,i+1/2,j} = q_{sy\,i,j} + 0.5\varphi(q_{sy\,i,j} - q_{sy\,i-1,j}),\ \ \overline{q}^{L}_{c\,i+1/2,j} = q_{c\,i,j} + 0.5\varphi(q_{c\,i,j} - q_{c\,i-1,j}) \tag{22e, f}$$

where φ represents the slope-limited function evaluated at cell (i, j) based on the flow and sediment data at the cell and its upwind and downwind neighbours, and the minmod slope limiter is used for better numerical stability (Hirsch 1990)

$$\varphi(r) = \max[0, \min(r, 1)] \tag{23}$$

where r is the ratio of successive gradients of the flow and the variable under consideration; for example, e.g., for η

$$r = \frac{\eta_{i+1,j} - \eta_{i,j}}{\eta_{i,j} - \eta_{i-1,j}} \tag{24}$$

Similar expressions can defined for q_{sx}, q_{sy}, q_c and h_s.

The interface values of the right-hand side of the cell interface $(i+1/2, j)$ are calculated in a similar way,

$$\overline{\eta}^{R}_{i+1/2,j} = \eta_{i,j} - 0.5\varphi(\eta_{i,j} - \eta_{i-1,j}),\ \ \overline{h}^{R}_{s\,i+1/2,j} = h_{s\,i,j} - 0.5\varphi(h_{s\,i,j} - h_{s\,i-1,j}) \tag{25a, b}$$

$$\overline{z}^{R}_{b\,i+1/2,j} = z_{b\,i,j} - 0.5\varphi(z_{b\,i,j} - z_{b\,i-1,j}),\ \ \overline{q}^{R}_{sx\,i+1/2,j} = q_{sx\,i,j} - 0.5\varphi(q_{sx\,i,j} - q_{sx\,i-1,j}) \tag{25c, d}$$

$$\overline{q}^{R}_{sy\,i+1/2,j} = q_{sy\,i,j} - 0.5\varphi(q_{sy\,i,j} - q_{sy\,i-1,j}),\ \ \overline{q}^{R}_{c\,i+1/2,j} = q_{c\,i,j} - 0.5\varphi(q_{c\,i,j} - q_{c\,i-1,j}) \tag{25e, f}$$

where φ is evaluated at cell $(i+1, j)$. The velocity components and volumetric sediment concentration are then calculated by

$$\bar{u}^{L}_{si+1/2,j} = \bar{q}^{L}_{sx\,i+1/2,j} \Big/ \bar{h}^{L}_{s\,i+1/2,j}, \quad \bar{u}^{R}_{si+1/2,j} = \bar{q}^{R}_{sx\,i+1/2,j} \Big/ \bar{h}^{R}_{s\,i+1/2,j} \tag{26a, b}$$

$$\bar{v}^{L}_{si+1/2,j} = \bar{q}^{L}_{sy\,i+1/2,j} \Big/ \bar{h}^{L}_{s\,i+1/2,j}, \quad \bar{v}^{R}_{si+1/2,j} = \bar{q}^{R}_{sy\,i+1/2,j} \Big/ \bar{h}^{R}_{s\,i+1/2,j} \tag{26c, d}$$

$$\bar{c}^{L}_{si+1/2,j} = \bar{q}^{L}_{c\,i+1/2,j} \Big/ \bar{h}^{L}_{s\,i+1/2,j}, \quad \bar{c}^{R}_{si+1/2,j} = \bar{q}^{R}_{c\,i+1/2,j} \Big/ \bar{h}^{R}_{s\,i+1/2,j} \tag{26e, f}$$

Based on the above interface values, the Riemann states can be sought for designing the non-negativity of water depth. As suggested by Liang (2010), a single bed elevation at the cell interface $(i+1/2, j)$ may be defined as

$$z_{b\,i+1/2,j} = \max(\bar{z}^{L}_{b\,i+1/2,j}, \bar{z}^{R}_{b\,i+1/2,j}) \tag{27}$$

The depth components of the Riemann states are then defined by

$$h^{L}_{s\,i+1/2,j} = \max(0, \bar{\eta}^{L}_{s\,i+1/2,j} - z_{b\,i+1/2,j}), \quad h^{R}_{s\,i+1/2,j} = \max(0, \bar{\eta}^{R}_{s\,i+1/2,j} - z_{b\,i+1/2,j}) \tag{28}$$

which preserves positive water depth. The Riemann states of other flow variables can be obtained accordingly

$$\eta^{L}_{s\,i+1/2,j} = h^{L}_{s\,i+1/2,j} + z_{b\,i+1/2,j}, \quad q^{L}_{sx\,i+1/2,j} = \bar{u}^{L}_{s\,i+1/2,j} h^{L}_{s\,i+1/2,j} \tag{29a, b}$$

$$q^{L}_{sy\,i+1/2,j} = \bar{v}^{L}_{s\,i+1/2,j} h^{L}_{s\,i+1/2,j}, \quad q^{L}_{c\,i+1/2,j} = \bar{c}^{L}_{s\,i+1/2,j} h^{L}_{s\,i+1/2,j} \tag{29c, d}$$

$$\eta^{R}_{s\,i+1/2,j} = h^{R}_{s\,i+1/2,j} + z_{b\,i+1/2,j}, \quad q^{R}_{sx\,i+1/2,j} = \bar{u}^{R}_{s\,i+1/2,j} h^{R}_{s\,i+1/2,j} \tag{29e, f}$$

$$q^{R}_{sy\,i+1/2,j} = \bar{v}^{R}_{s\,i+1/2,j} h^{R}_{s\,i+1/2,j}, \quad q^{R}_{c\,i+1/2,j} = \bar{c}^{R}_{s\,i+1/2,j} h^{R}_{s\,i+1/2,j} \tag{29g, h}$$

According to Liang (2010), for a dry-bed application, a numerical technique is needed to preserve the well-balanced solutions. For example, the bed elevation and the stage component of Riemann states are locally and instantaneously modified by subtracting Δz from the original values. And $\Delta z = \max[0, (z_{b\,i+1/2,j} - \bar{\eta}^{L}_{s\,i+1/2,j})]$ denotes the difference between the actual and fake water surface level at the cell interface $(i+1/2, j)$.

$$z_{b\,i+1/2,j} \leftarrow z_{bi+1/2,j} - \Delta z \tag{30a}$$

$$\eta^{L}_{s\,i+1/2,j} \leftarrow \eta^{L}_{s\,i+1/2,j} - \Delta z,\ \ \eta^{R}_{s\,i+1/2,j} \leftarrow \eta^{R}_{s\,i+1/2,j} - \Delta z \tag{30b, c}$$

The bed slope term S_b^k is discretised using the method proposed by Liang (2010). The procedure for the x-direction is outlined below; that for the y-direction is similar.

$$-g\eta_s \frac{\partial z_b}{\partial x} = -g\overline{\eta}_s \left(\frac{z_{b\,i+1/2,j} - z_{b\,i-1/2,j}}{\Delta x} \right) \tag{31}$$

where $\overline{\eta}_s = \left(\eta^{R}_{s\,i-1/2,j} + \eta^{L}_{s\,i+1/2,j} \right)$

Eq. (1) for the clear-water flow layer can be solved in a similar procedure as Eq. (2).

The current numerical scheme is explicit and its stability is controlled by the Courant-Friedrichs-Lewy condition. The time step is given by

$$\Delta t = C_r \min\left(\frac{\Delta x}{\left|u_{wi,j}\right| + \left(gh_{wi,j}\right)^{1/2}}, \frac{\Delta y}{\left|v_{wi,j}\right| + \left(gh_{wi,j}\right)^{1/2}}, \frac{\Delta x}{\left|u_{si,j}\right| + \left(gh_{si,j}\right)^{1/2}}, \frac{\Delta y}{\left|v_{si,j}\right| + \left(gh_{si,j}\right)^{1/2}} \right) \tag{32}$$

TEST CASES

A series of experimental cases are solved to verify the present 2D double layer-averaged model, concerning turbidity currents due to lock-exchange and sustained inflow. In the present work, a fixed uniform mesh is adopted, and the spatial step is sufficiently fine to ensure mesh independence of the solution, i.e., essentially equivalent solutions are obtained with an even finer mesh. The Courant number C_r is 0.5 and bed porosity $p =$ 0.4 is adopted for all the test cases.

Lock-exchange Turbidity Currents

A series of experiments were conducted at University of Cambridge to enhance the understanding of the depositional characteristics and front propagation of lock-exchange turbidity currents, including 1D (Hallworth and Huppert 1998) and 2D (Bonnecaze et al. 1995) cases. The present 2D double layer-averaged model is tested against some of the experiments with relatively low sediment

346 concentrations, in which the turbidity currents can be considered as Newtonian fluids approximately.
347 Here, the 2D experimental axisymmetric turbidity currents by Bonnecaze et al. (1995) are revisited. A
348 plan view sketch of the flume is given in Figure 1. The flume consists of a rectangular part (0.038 m
349 wide and 0.306 m long) and a radial part (the width expands from 0.038 to 0.294 m within 1.83 m). A
350 lock gate is placed at the centre of the rectangular part, which separates the flume-filled
351 water-sediment mixture on the left side and clear water on the right side. The initial thickness of the
352 turbidity volume and clear water is 0.14 m. Turbidity currents are initiated by instantaneous vertical
353 withdrawal of the lock gate. The medium diameter of the sediment was 37 μm and its density was
354 3217 kg/m^3. Three runs are conducted with different initial sediment concentrations: c_{s0}= 0.019, 0.01
355 and 0.005. E_s is calculated using Eq. (12). The spatial steps Δx and Δy are both 0.005 m. The
356 bed roughness n_b and the interface roughness n_w are determined by fitting to measured front
357 location. It is found that n_b = 0.015 m$^{-1/3}$ and n_w = 0.005 m$^{-1/3}$ lead to satisfactory agreements with
358 measured data.

359 Fig. 2 shows the turbidity current front location against time and the final deposit density plotted
360 versus the radial distance, respectively. The radial distance is measured from the ghost origin as
361 indicated in Fig. 1, which is set to be the intersection of the extended walls of the radial flume. From
362 Fig. 2, the computed advance of current front and the final deposition density by the present model
363 agree with measured values rather well.

364 When the lock gate is removed, the plunging of turbidity volume leads to the formation of
365 turbidity currents. The thickness of the current decreases sharply with the propagation of the current.
366 Initially the turbidity current advances fast, but decelerates gradually in time [Fig. 2(a)]. The higher
367 the initial sediment concentration, the faster the turbidity current propagates, and naturally more
368 sediment is deposited [Fig. 2(b)]. The final deposition density has a maximum value near the ghost
369 origin point and decreases asymptotically along the channel.

370 Lock-exchange turbidity currents are formed by the sudden release of a fixed volume of turbid
371 water, and driven by difference in density from the ambient water, without any inflow at the upstream
372 or outflow at the downstream boundary. Physically, double layer-averaged models are generally

applicable, though a single layer-averaged model has been suggested to be approximately workable in deep ambient water (Bonnecaze et al. 1993). Nevertheless, it is recognized that lock-exchange turbidity currents substantially differ from reservoir turbidity currents that are generally controlled by both the upstream and downstream boundary conditions. Thus the following test is warranted of the present model against reservoir turbidity currents subject to sustained inflow (and in some cases outflow) at a laboratory scale.

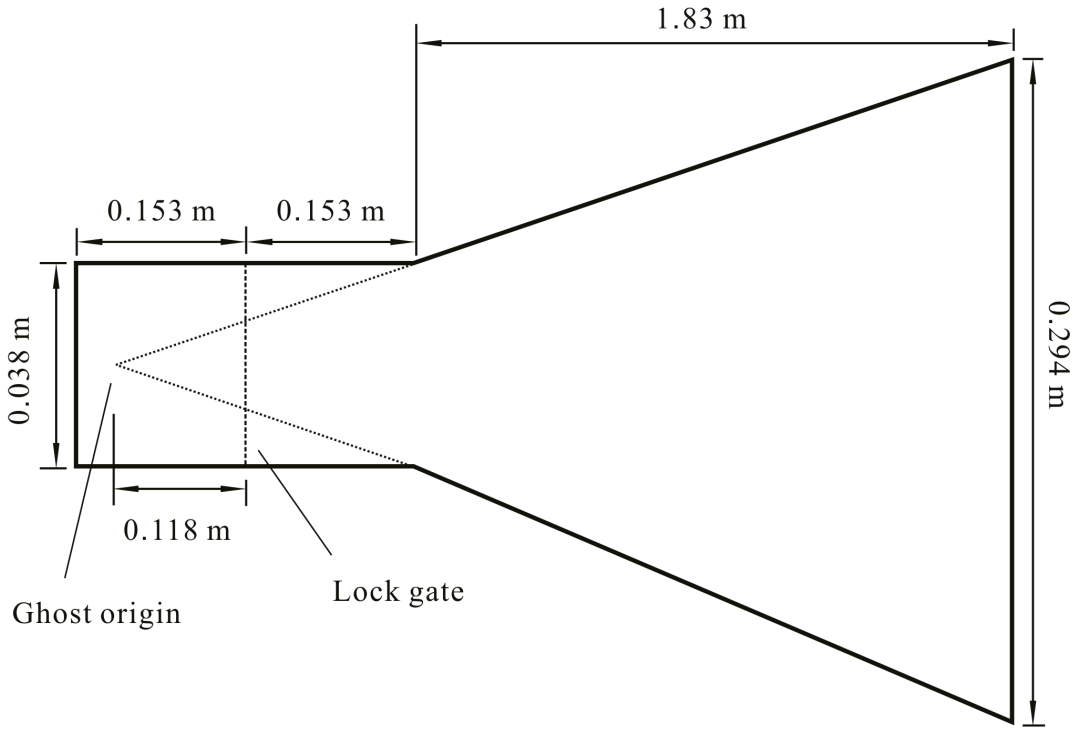

Fig. 1. Plan view sketch of experimental flume (adapted from Bonnecaze et al. 1995)

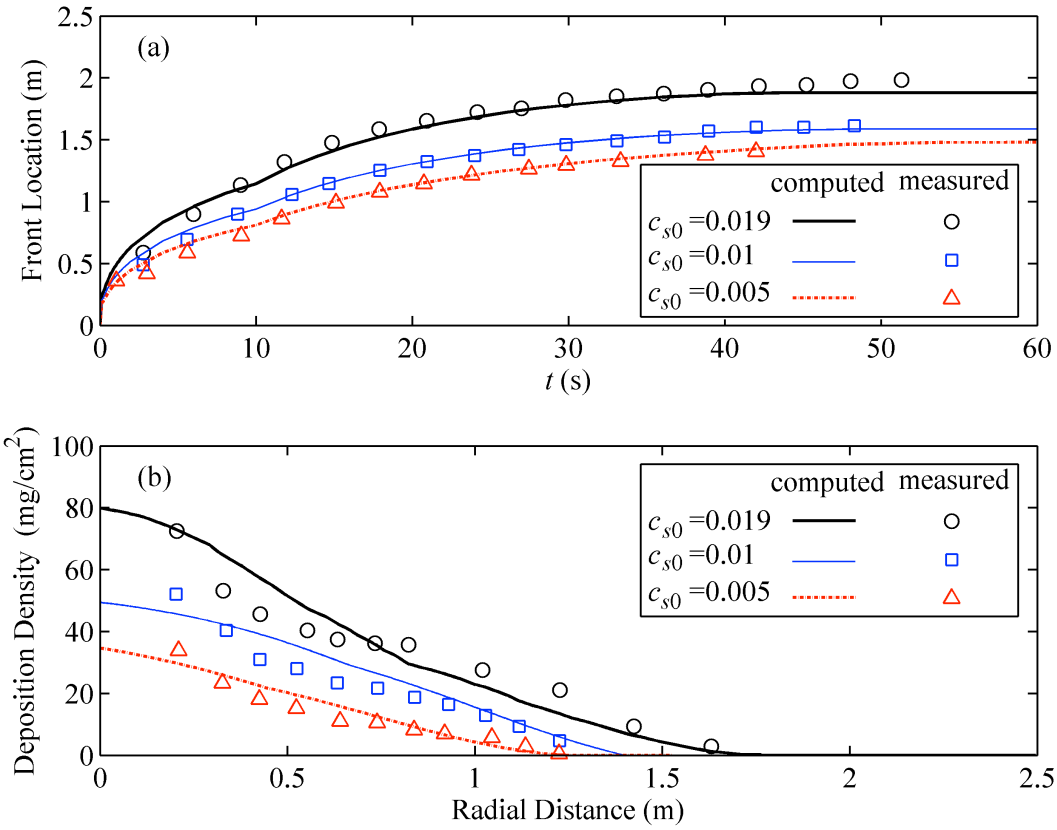

Fig. 2. Numerical solutions compared with measured data for 2D lock-exchange turbidity current: (a) front location, and (b) final deposition density

Turbidity Currents Due to Sustained Inflow

This subsection focuses on the turbidity currents due to sustained inflow from the upstream, and in some cases subject to an outflow at the downstream, in contrast to lock-exchange turbidity currents considered above. Lee and Yu (1997) carried out a series of experiments in a transparent flume of dimensions 20 m×0.2 m×0.6 m and bed slope 0.02. A receiving tank was installed at the end of sloping section. The suspended material was kaolin having a specific gravity of 2.65 and a mean particle size of 6.8 μm. During the experimental process, the flume was first filled with clear water to form a reservoir, and then open-channel sediment-laden flow was released from the head tank. In most runs, the outflow discharge q_{out} was set equal to the inflow discharge q_{in}, while in some other runs, q_{out} was kept zero all the time or from some instant. The inflow discharge and its sediment concentration were kept constant in each run of the experiments.

To demonstrate the performance of the model, Series B and C are revisited. Series B was performed to investigate the migration of the plunge point and corresponding variations of the plunge criteria, while Series C was designed to investigate the length of the plunge region and the hydraulic characteristics of the turbidity current over a long distance. The inflow conditions for all revisited experimental runs are summarized in Table 1.

It is noted that the significant value of the systematic experiments by Lee and Yu (1997) has not been sufficiently exploited to support the development of analytical and computational models for reservoir turbidity currents. Only one run (Series C- TC 8) has ever been simulated with a vertical 2D model based on the Reynolds-averaged Navier-Stokes equations and κ - ε turbulence closure (Kassem and Imran 2001). In principle, the formation of the turbidity current could be resolved by this model, which, however, was not explicitly evaluated. Also, the impacts of the outflow as related to Series B - PP4 were not resolved at all, possibly because the flow system becomes unsteady and the computing cost is too high. There has been a plethora of single layer-averaged models (e.g., Choi 1998; Bradford and Katopodes 1999a, b; Sequeiros et al. 2009; Hu et al. 2012; Lai and Wu 2013), but none has been verified against the observed data of Lee and Yu (1997).

For this modelling exercise, the computational domain consists of the sloping section without including the receiving tank at the far downstream end of the flume. It is assumed that the discharge at the end of the sloping section is equal to the outflow discharge because the receiving tank is rather short. At the inlet boundary, there was no clear-water flow layer; and as the inflow discharge was specified, the depth and velocity of the sediment-laden flow were determined by the method of characteristics. A downstream boundary condition is not required for the turbidity current as the computation is automatically terminated once the current reaches the downstream boundary. For the outlet boundary condition of the clear-water flow layer, the depth and velocity were determined by the method of characteristics as the outflow discharge was specified. The spatial step Δx is 0.025 m. The bed roughness n_b and the interface roughness n_w are first calibrated using measured data from Series B - PP 1, and then directly applied for the other cases. It is found that interface roughness $n_w =$ 0.005 $m^{-1/3}$ s and bed roughness $n_b =$ 0.015 $m^{-1/3}$ s lead to satisfactory agreements with measured data. E_s is determined according to Eq. (12) as ψ ranges between 4.0 and 20.0, which means partial

426 erosion and deposition. It is also found that the maximum value of bed deformation is merely 3.4×10^{-5}

427 m (not shown). Here, x_p is the distance between the plunge point and flume entrance, h_p is the

428 current thickness at the plunge point and $\mathrm{F}_p = u_s / \sqrt{g'_p h_p}$, is the densimetric Froude number.

429

430 **Table 1** Summary of inflow conditions for all revisited experimental runs

Run	Series B		Run	Series C	
	Inflow conditions			Inflow conditions	
	q_{in}	c_s		q_{in}	c_s
	(cm^2/s)	(10^{-3})		(cm^2/s)	(10^{-3})
PP 1	23.5	3.71	TC 1	24.23	4.36
PP 2	42.25	3.71	TC 2	24.76	7.16
PP 3	70.56	2.51	TC 3	42.25	3.63
PP 4	85.10	2.00	TC 4	41.63	7.27
PP 5	86.74	3.86	TC 5	41.78	10.78
PP 6	100.21	3.27	TC 6	68.01	2.36
PP 7	86.01	5.61	TC 7	68.22	4.27
PP 8	99.64	4.98	TC 8	67.90	6.67
PP 9	101.20	6.60	TC 9	68.28	8.59
PP 10	134.46	4.85	TC 10	85.27	2.10
			TC 11	85.45	3.88
			TC 12	85.21	5.43
			TC 13	84.70	7.37
			TC 14	97.56	3.10
			TC 15	97.52	4.73
			TC 16	97.40	5.99
			TC 17	96.47	7.81
			TC 18	116.07	6.81

431

432 *Turbidity current formation and propagation*

433 Fig. 3 illustrates the formation and propagation processes of the turbidity current with unit-width

434 inflow discharge 97.52 cm^2/s and volumetric sediment concentration 4.73×10^{-3}, in relation to Run TC

435 15 (Table 1). It is noted that upstream the plunge point, the interface is actually the water surface,

436 characterizing that there is no clear water flow and thus the flow is essentially subaerial open-channel

437 sediment-laden flow. As the turbid water flows forward, a separation becomes pronounced from the

clear water in the reservoir [Fig. 3(b)]. Then the sediment-laden flow plunges to the bottom and begins to move as an underflow, i.e., turbidity current [Fig. 3(c-d)], of which the upper boundary is indicated by the "interface." Succinctly, the formation process of reservoir turbidity current is characterized by the transition from subaerial open-channel sediment-laden flow to subaqueous turbid flow. At this stage, the plunge point is unstable and still moves forward. By $t > 160$ s approximately, the plunge point stabilizes and the current advances with a bulge-shaped head and elongated body.

It is noted that when the upper layer vanishes, Eq. (2) for the lower layer reduces to a system of equations of a traditional shallow water hydrodynamic and sediment model for open-channel sediment-laden flows (e.g., Cao et al. 2011), which differs from that of a single layer-averaged model for turbidity currents (Hu et al. 2012). This exactly explains why the present double layer-averaged model can resolve the formation process of reservoir turbidity current, characterized by the transition from open-channel sediment-laden flow to subaqueous turbidity current.

To date, the authors are not aware of any previous layer-averaged models that can resolve the formation process of the turbidity currents due to sustained inflow, though systematic experimental observations have been available for long since Lee and Yu (1997). Most plausibly, this is because the currently available single layer-averaged models (e.g., Choi 1998; Bradford and Katopodes 1999a, b; Sequeiros et al. 2009; Hu et al. 2012; Lai and Wu 2013) simply do not have the capability of resolving the interactions between the open-channel sediment-laden flow input from the upstream and the ambient water in the reservoir, irrespective of whether the later is static or flowing as dictated by the outflow in relation to the reservoir operation schemes. This is most telling that the present double layer-averaged is warranted if the whole processes of reservoir turbidity currents are to be sufficiently resolved. This is further demonstrated in the following subsections, as compared against the observed data of Lee and Yu (1997) and the analytical formulations of Dai and Garcia (2009) and Li et al. (2011). Presented below are the characteristics at the plunge point, the streamwise profiles of the thickness, mean velocity and sediment concentration of the turbidity currents, as well as the impacts of the outflow at the downstream.

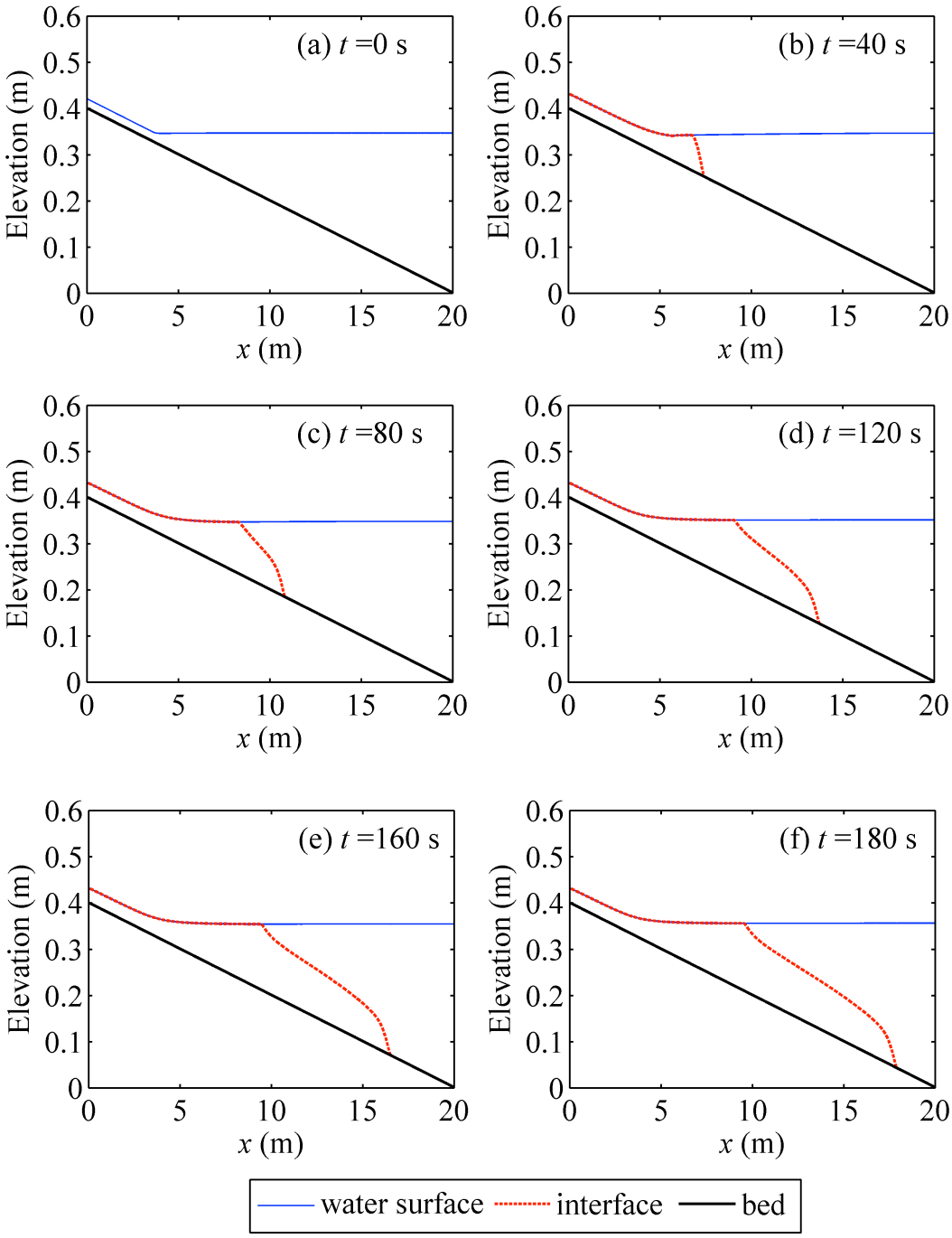

Fig. 3. Turbidity current formation and propagation (Series C - TC 15)

Characteristics at the plunge point

Shown in Tables 2 and 3 are the parameters at the incipient and stable plunge points for Series B and Series C, corresponding to different inflow conditions. The analytical densimetric Froude number solution at the incipient plunge point developed by Li et al. (2011) is based on energy balance and

473 includes the effects of the bed slope, sediment concentration and the discharge of the turbidity current.
474 Dai and Garcia (2009) analyzes the densimetric Froude number at the stable plunge point by taking
475 into account the bed slope and inflow conditions. Tables 2 and 3 clearly illustrate that the computed
476 results match the measured data and analytical results very well. It is shown that F_p at the incipient
477 plunge point ranges approximately between 0.9 and 1.0, while F_p at the stable plunge point varies
478 around 0.6. Thus the incipient plunging occurs when F_p equals to 0.9~1.0, and F_p reduces as the
479 plunge point migrates downstream. The plunge point finally reaches a stable condition, where F_p
480 equals 0.6. And the h_p and F_p at the incipient plunge point as well as x_p, h_p and F_p at the
481 stable plunge point increase with the increase of the inflow discharge, but decrease with the increase
482 of sediment concentration. This is mainly because larger discharge or smaller sediment concentration
483 corresponds to smaller value of Ri and thus induces more water entrainment.

484 Fig. 4 shows the computed relationship between h_p and $(q_p^2/g_p')^{1/3}$ for Series B, including
485 those not only at the incipient and stable plunge points, but also in between them. The theoretical
486 results at the incipient plunge point according to Li et al. (2011) and at the stable plunge point due to
487 Dai and Garcia (2009) are also included. The two dash lines represent respectively the incipient and
488 stable plunge points, corresponding to F_p = 1.0 and 0.6 proposed by Lee and Yu (1997). Echoing
489 Tables 2 and 3, the computed results from the present model agree with the analytical results based on
490 Li et al. (2011) and Dai and Garcia (2009) and also the observed data of Lee and Yu (1997) rather well.
491 Fig. 5 shows the temporal variation of the plunge point location for three typical cases in Series B. It is
492 seen that the location of the stable plunge point and also the time from the incipient to stable plunge
493 point are distinct as the inflow discharge and sediment concentration vary. For a specific case (Series
494 B- PP 4), the densimetric Froude number F_p decreases and the plunge depth h_p increases with
495 time, and eventually both reaches stable values (Fig. 6).

496

497

498 **Table 2** Parameters at incipient and stable plunge points (Series B)

RUN	Incipient				Stable			
	h_p (cm)		F_p		h_p (cm)		F_p	
	meas.	comp.	Li et al.	comp.	meas.	comp.	Dai & Garcia	comp.
PP 1	5.36	5.31	0.81	0.86	6.87	6.80	0.62	0.63
PP 2	7.40	7.37	0.96	0.97	9.28	9.39	0.65	0.62
PP 3	10.25	9.97	0.96	0.96	13.85	14.12	0.69	0.68
PP 4	12.56	12.48	1.02	1.03	17.15	17.25	0.64	0.64
PP 5	10.57	10.46	0.98	0.99	13.19	12.95	0.70	0.68
PP 6	13.54	13.63	0.95	0.97	16.32	16.40	0.72	0.69
PP 7	9.68	9.45	0.97	0.98	12.63	12.52	0.64	0.64
PP 8	12.84	12.43	0.97	0.99	14.37	14.60	0.66	0.67
PP 9	10.68	10.26	1.05	1.06	13.45	13.69	0.64	0.64
PP 10	12.68	12.38	0.94	1.03	18.09	17.95	0.68	0.67

499

500 **Table 3** Parameters at incipient and stable plunge points (Series C)

Run	Incipient				Stable			
	F_p		x_p		h_p		F_p	
	Li et al.	comp.	meas.	comp.	meas.	comp.	Dai & Garcia	comp.
TC 1	0.85	0.87	6.03	6.025	6.64	7.88	0.62	0.61
TC 2	0.89	0.90	5.52	5.50	5.62	6.43	0.64	0.63
TC 3	0.96	0.98	7.10	7.12	8.91	9.73	0.66	0.68
TC 4	0.95	0.94	6.29	6.31	7.17	7.94	0.65	0.67
TC 5	0.97	0.95	10.05	10.12	14.31	15.18	0.63	0.61
TC 6	0.99	0.96	10.05	10.12	14.31	15.18	0.63	0.61
TC 7	1.01	1.0	9.65	9.60	11.31	12.46	0.59	0.58
TC 8	0.98	0.99	8.05	8.03	10.53	11.13	0.65	0.62
TC 9	0.97	0.97	7.76	7.68	10.02	10.89	0.64	0.63
TC 10	0.99	0.96	11.24	11.26	17.04	17.85	0.66	0.65
TC 11	0.98	0.95	10.13	10.09	14.49	15.26	0.65	0.64
TC 12	1.02	1.03	9.46	9.56	12.97	13.69	0.64	0.66
TC 13	0.99	0.96	8.58	8.63	11.16	11.86	0.66	0.67
TC 14	0.98	0.97	10.96	10.98	16.51	17.20	0.67	0.65
TC 15	1.01	0.99	10.04	10.03	14.29	14.96	0.65	0.66
TC 16	0.99	0.98	9.55	9.68	13.18	14.29	0.67	0.64
TC 17	1.02	1.03	8.71	8.74	11.44	12.35	0.63	0.65
TC 18	0.99	0.96	9.68	9.78	9.68	10.03	0.67	0.65

501

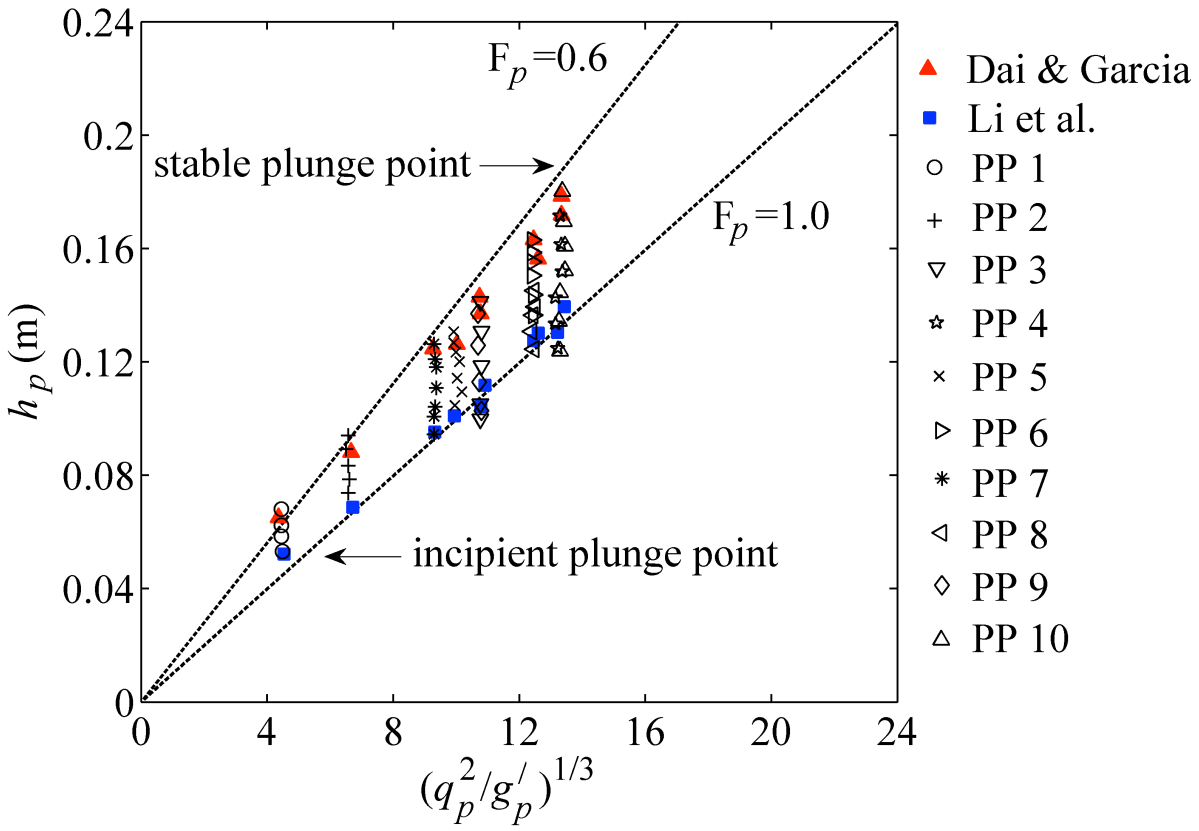

502

503 **Fig. 4.** Computed turbidity current thickness at plunge point compared with analytical formulations,

504 with two dash lines representing the incipient and stable plunge points due to Lee and Yu (1997)

505

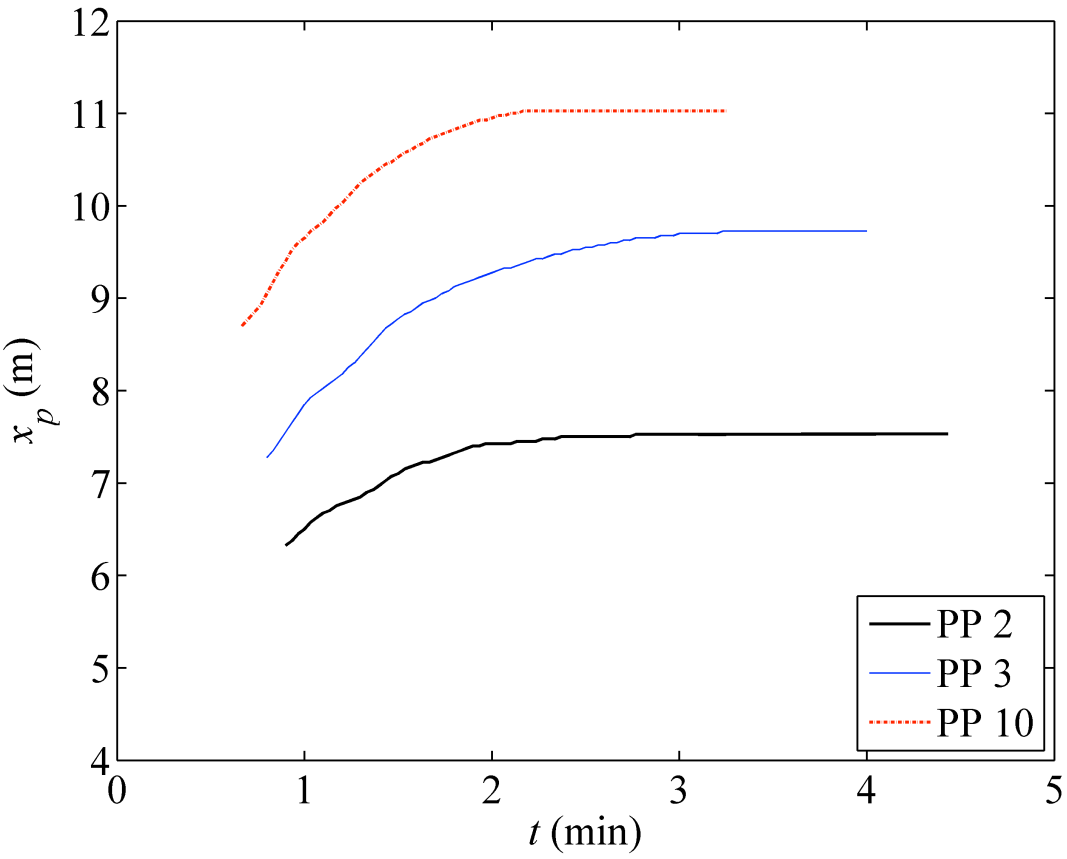

506

507 **Fig. 5.** Temporal variation of plunge point location

508

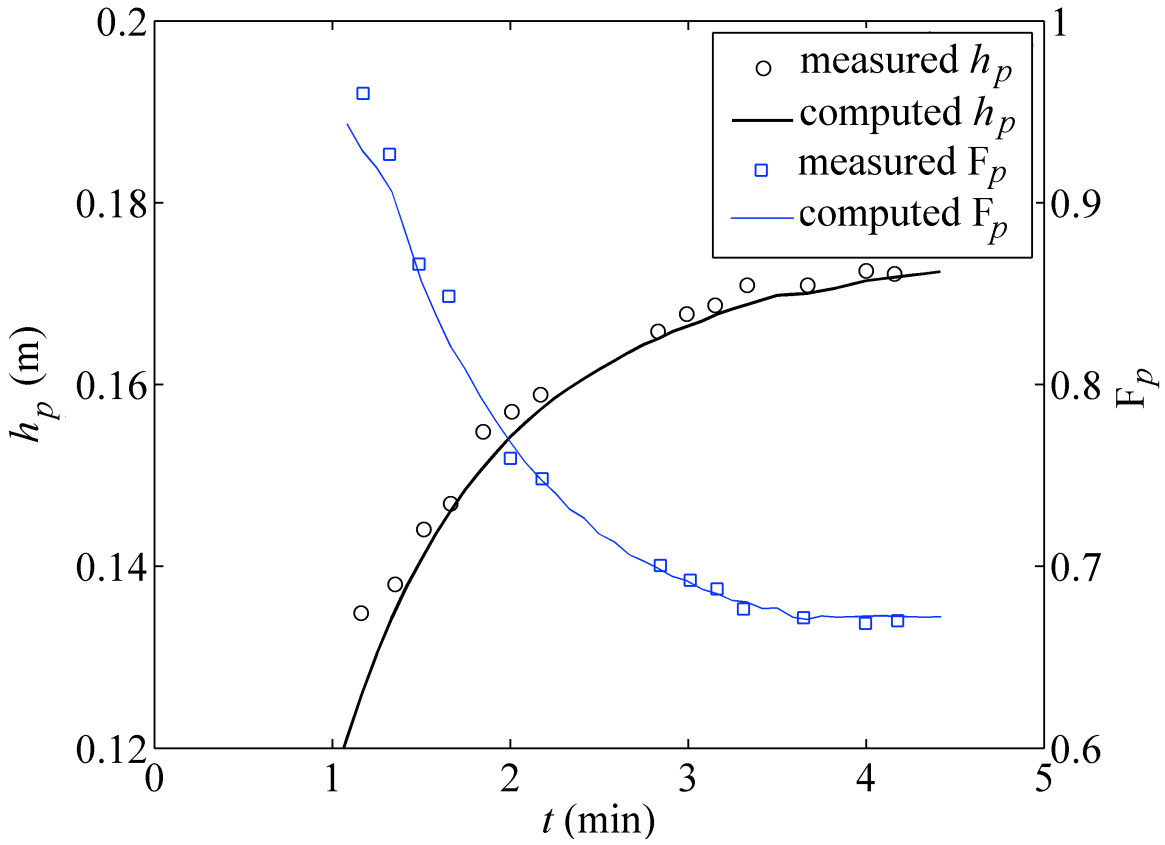

509

510 **Fig. 6.** Computed densimetric Froude number and turbidity current thickness at plunge point

511 compared with measured data (Series B-PP4)

512

513 *Non-dimensional profiles of turbidity currents*

514 Fig. 7 shows the spatial variation of dimensionless current thickness, velocity and sediment
515 concentration computed by the present model along with measured data. Here, the data from Runs TC
516 5, TC 8, TC 12 and TC 15 at two selected cross-sections located at 11.3 m and 13.3 m respectively
517 from the inlet of the flume are considered. Due to water entrainment, the discharge of the turbidity
518 currents increases longitudinally and hence can be treated as an index of the distance from the plunge
519 point. The data at $x =$ 11.3 m in run TC 5 are used as the reference values to nondimensionalize the
520 thickness, velocity, sediment concentration and discharge of the turbidity currents, which are
521 represented by $\hat{h}_s$, $\hat{u}_s$, $\hat{c}_s$ and $\hat{q}_s$, respectively. It is seen from Fig. 7 that because of water
522 entrainment, the thickness of turbidity currents increases longitudinally and thus the velocity and
523 sediment concentration reduce accordingly. Overall, the observed non-dimensional thickness, velocity

524 and sediment concentration profiles of the turbidity currents are well reproduced by the present model.

525

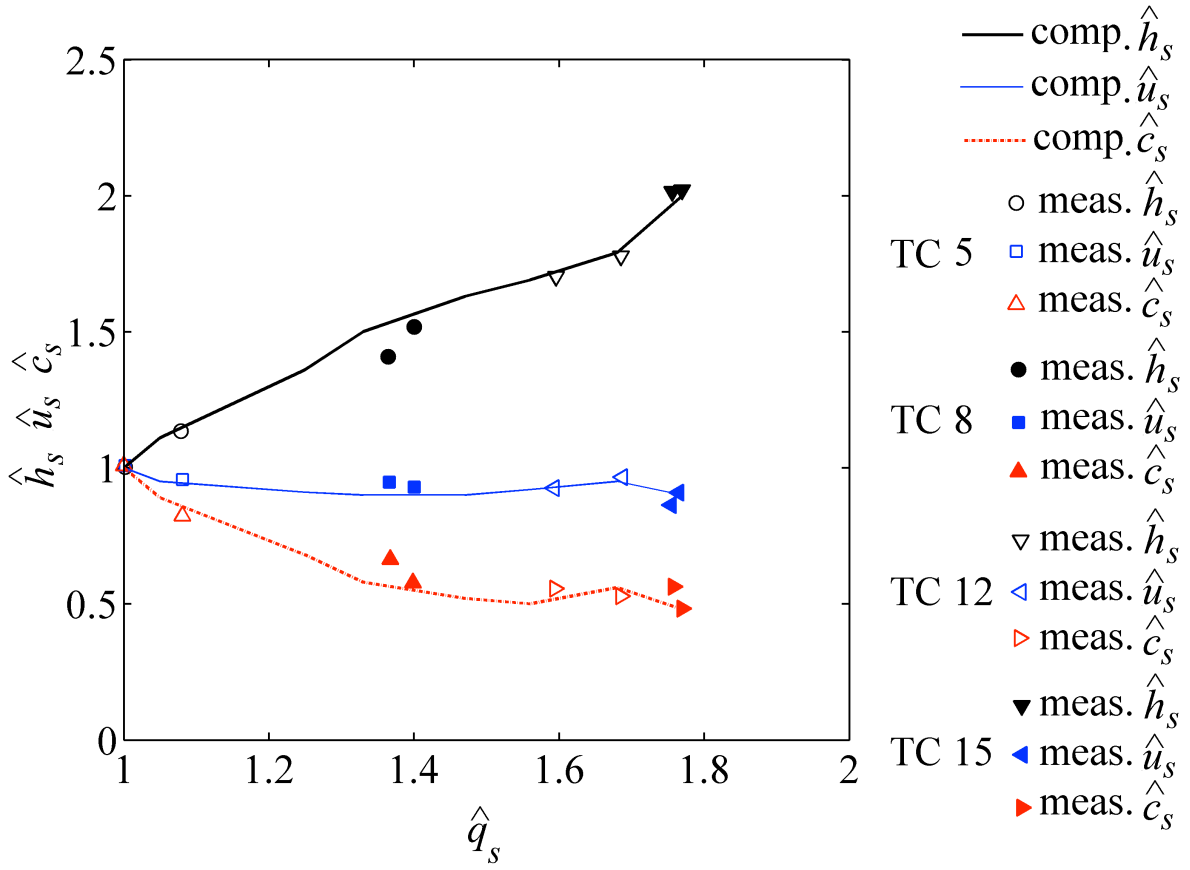

526

527 **Fig. 7.** Computed dimensionless turbidity current thickness, velocity and sediment concentration

528 compared with measured data

529

530 *Impacts of downstream boundary conditions on turbidity currents*

531 Fig. 8 illustrates the impacts of downstream boundary conditions on the turbidity currents in
532 relation to Series B - PP4. The impacts are represented by variations in the plunge flow depth, plunge
533 location and front location of the turbidity current. It is shown in Fig. 8 that if the outflow is cutoff
534 from the initial state, the plunge point has not yet reached a stable state within the time period
535 considered. Likewise, the stable plunge point becomes unstable as the outflow is terminated at 4.33
536 min. As the outflow increases, the water level in the reservoir will get lower. Most notably, an outflow
537 of clear water in the upper layer generally leads to a decrease in the plunge depth [Fig. 8(a)], migration

538 of the plunge location downstream [Fig. 8(b)], and acceleration of the propagation [Fig. 8(c)] of the
539 turbidity current, and vice versa. Physically, a clear-water outflow facilitates a certain flow velocity of
540 the upper layer, which leads to less interface resistance (Eq. 6) to the turbidity current and reduced
541 water entrainment (Eq. 8).

542 From Figs. 4, 6, 7 and 8(a) as well as Tables 2 and 3, the computed results by the present model
543 agree with measured values rather well, though subtle differences are spotted. This suggests that the
544 turbidity currents are reasonably well resolved by the present model.

545

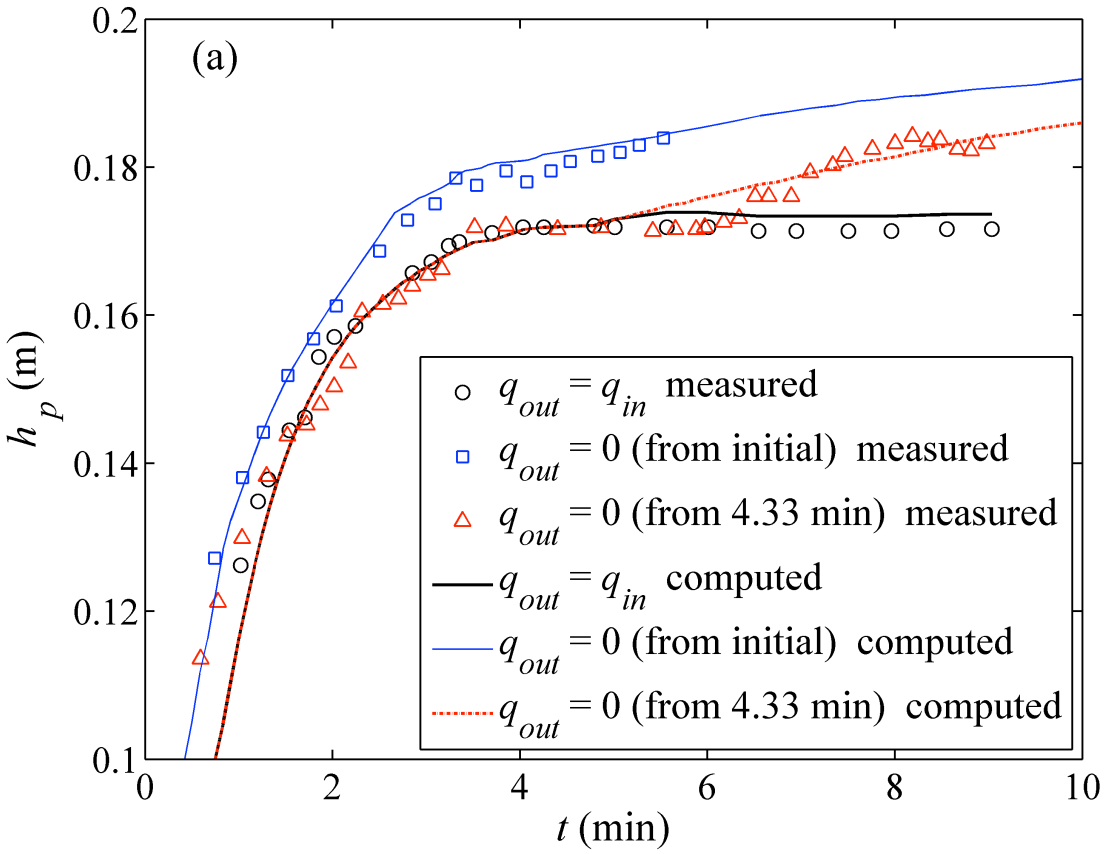

546

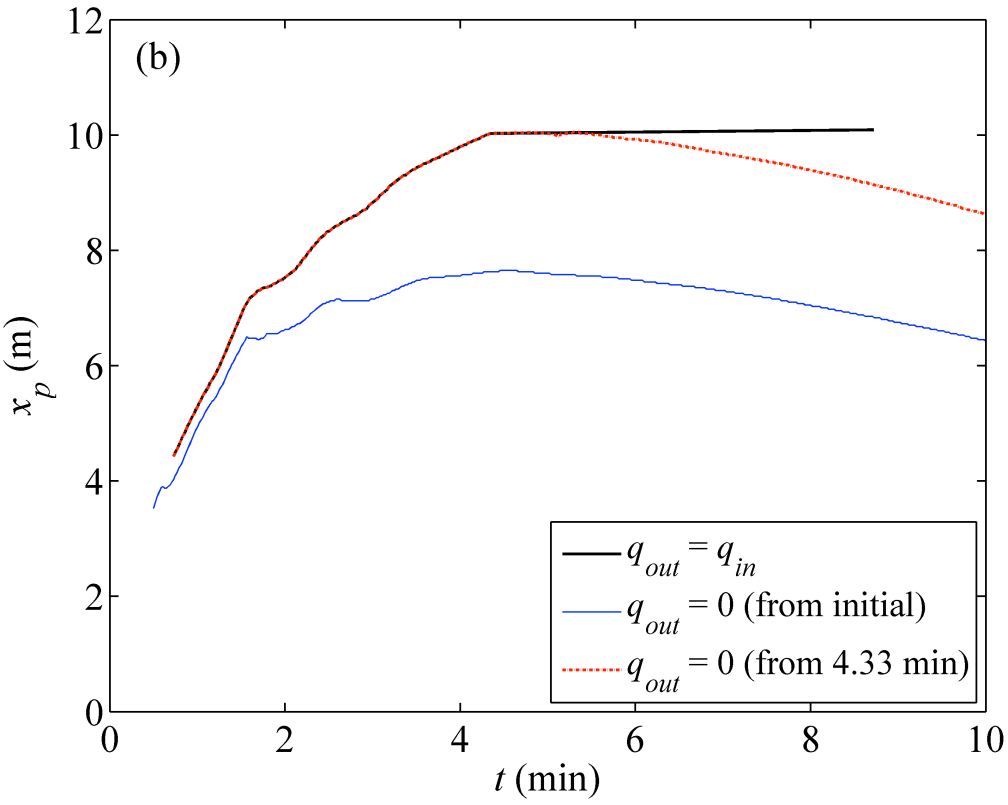

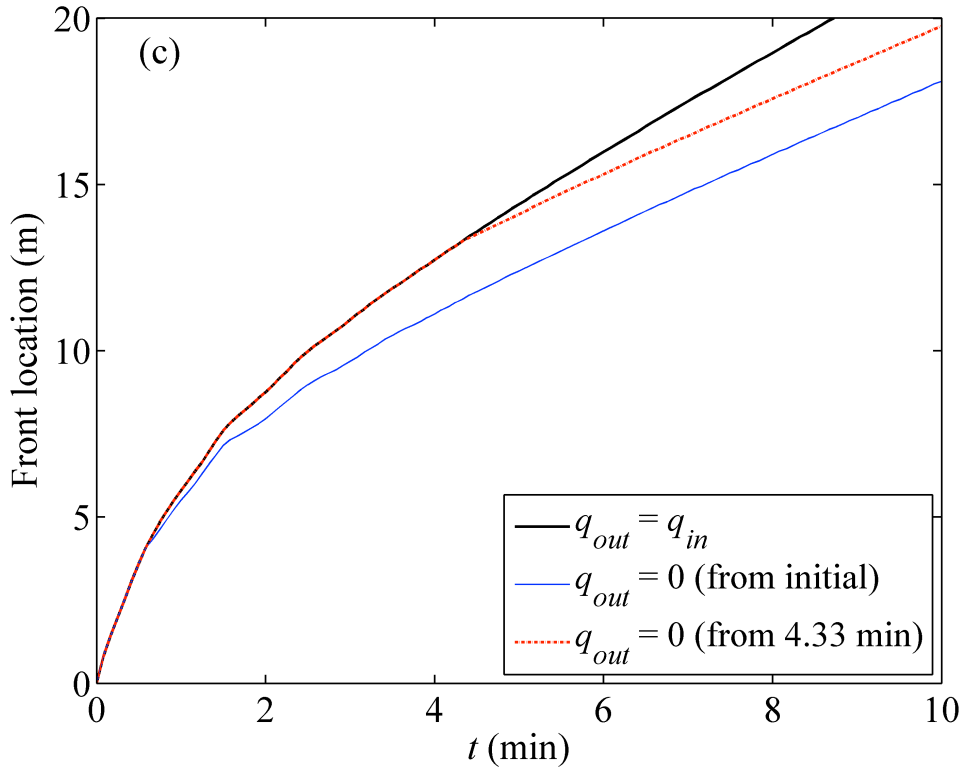

Fig. 8. Impacts of downstream boundary conditions: (a) computed turbidity current thickness at plunge point compared with measured data, (b) computed plunge location, and (c) computed front location (Series B -PP 4)

552

553 *Sediment flushing efficiency*

554 It is interesting to evaluate sediment flushing efficiency of a reservoir. In general, it is defined as
555 the ratio of the bulk sediment volume V_{si} input from the inlet of the reservoir to that (V_{so}) carried
556 away through the downstream boundary. Here V_{si} and V_{so} are calculated by

557 $$V_{si}(t) = \int (h_s u_s c_s)_{inlet} dt, \qquad V_{so}(t) = \int (h_s u_s c_s)_{outlet} dt \tag{33a, b}$$

558 It is noted that Lee and Yu (1997) focused on the turbidity currents, whereas an evaluation of
559 sediment flushing efficiency was missing. In their experiments, no bottom outlet was placed for
560 sediment flushing at the downstream boundary (i.e., the end of the sloping section of the experimental
561 flume). Here the experimental runs Series B - PP4 (Lee and Yu 1997) are extended to facilitate
562 numerical investigation of the impacts of reservoir operation on sediment flushing. All the model
563 parameters are kept the same as used in subsection just above (Fig. 8). It is assumed that at the
564 downstream boundary, there is a 4 cm-high bottom outlet on the bed, which has a presumed maximum
565 (unit-width) discharge of 42.55 cm^2/s. When the turbidity current reaches the downstream boundary,
566 the bottom outlet is opened for sediment flushing, while the total outflow discharge (including
567 clear-water flow and possibly turbidity current) remains the same as that in the experiments by Lee
568 and Yu (1997). At the downstream boundary, before the arrival of the turbidity current, the depth and
569 velocity of the clear-water flow layer are determined by the method of characteristics according to the
570 total outflow discharge, as no downstream boundary condition is needed for the turbidity current.
571 When the turbidity current has reached the bottom outlet, its respective discharge is equal to the
572 maximum of the bottom outlet if the upper surface of the turbidity current is level with or higher than
573 that of the bottom outlet; otherwise it is equal to a proportion of the maximum discharge of the bottom
574 outlet calculated by the turbidity current thickness relative to the height of the bottom outlet. If the
575 turbidity current is under subcritical regime, its depth and velocity are determined by the method of
576 characteristics in line with its respective outflow discharge (q_s); otherwise no downstream boundary
577 condition is needed. Meanwhile the depth and velocity of the clear-water flow layer are determined by
578 the method of characteristics based on its respective discharge (= $q_{out} - q_s$).

579 Fig. 9 shows the sediment flushing efficiencies for the extended cases adapted from Series B -
580 PP4 of Lee and Yu (1997). In general, sediment flushing commences as the turbidity current reaches
581 the bottom outlet, and the flushing efficiency increases with time, which clearly requires sustained
582 inputs of water and sediment from the inlet. If the clear-water outflow is cutoff from the initial state or
583 after 4.33 min, the sediment flushing efficiency decreases. Generally, the sooner the clear-water
584 outflow is cutoff, the less the sediment flushed out of the reservoir. Physically, the clear-water outflow
585 accelerates the propagation of the turbidity current (Fig. 8c), which leads to an increase in the amount
586 of sediment flushed out and therefore enhanced sediment flushing efficiency.

587 It follows that an appropriate clear-water outflow not only favours the turbidity current
588 propagation (Fig. 8c), but also is conducive to improving sediment flushing efficiency (Fig. 9). This is
589 undoubtedly of significance for developing optimal sediment management schemes for reservoirs on
590 the Yellow River in China and others worldwide, which suffer from severe sedimentation problems. In
591 a way, it adds to the current understanding of the effects of distinct reservoir operation schemes on
592 sedimentation mitigation (Fan and Morris 1992a, b). Nevertheless, more detailed investigations are
593 necessary to delimit quantitatively the impacts of reservoir operation schemes on sediment flushing by
594 means of turbidity currents. This certainly holds for the Xiaolangdi Reservoir, for which a case study
595 is presented below. Particularly, it remains to be unraveled if an excessive clear-water outflow would
596 spoil the turbidity currents that have already formed, as a result of Kelvin-Helmholtz instability.

597 Equally importantly, the impacts of the downstream boundary conditions on turbidity currents are
598 in essence substantiated by the clear-water outflow through spillway and flood diversion, which is
599 usually determined by the reservoir operation scheme. These significant impacts clearly tell that
600 previous single layer-averaged models (e.g., Choi 1998; Bradford and Katopodes 1999a, b; Sequeiros
601 et al. 2009; Hu et al. 2012; Lai and Wu 2013) are inadequate for applications in such cases because the
602 clear-water flow is not modeled at all. The advantage (enhanced capability) of the present double
603 layer-averaged model is evident.

604

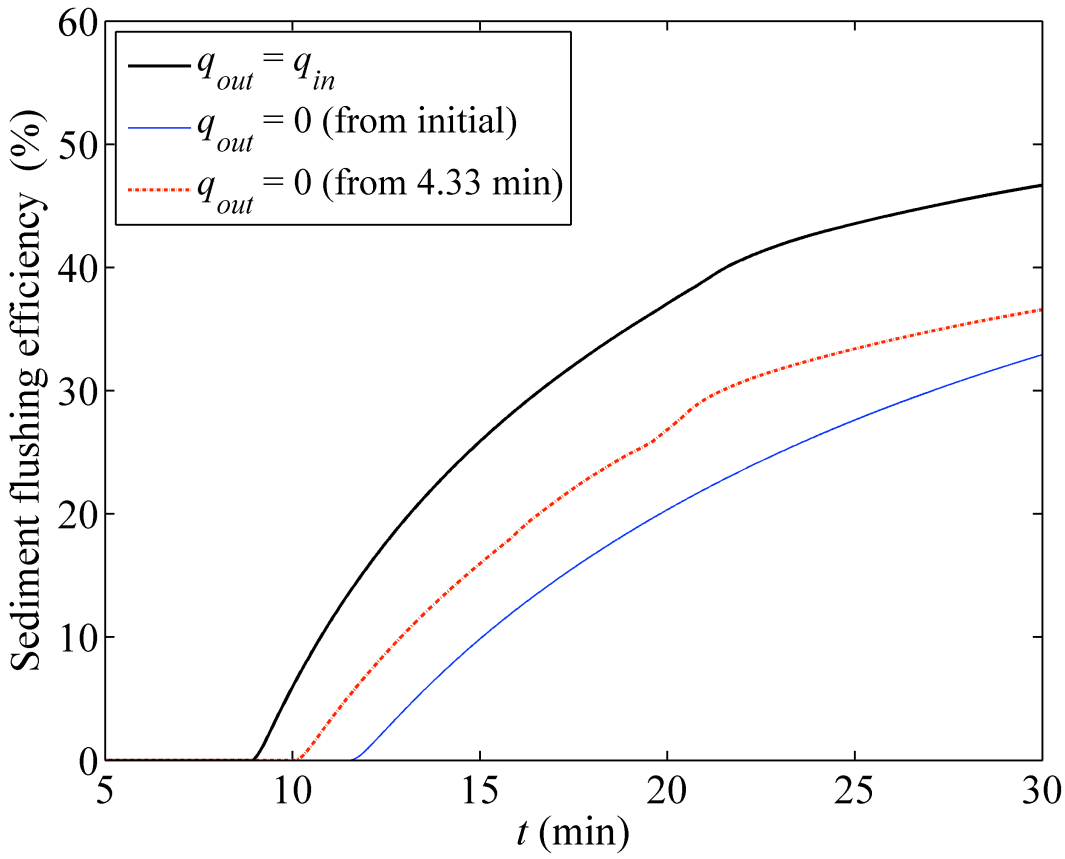

605

606 **Fig. 9.** Sediment flushing efficiencies for extended cases

607

608 **PILOT STUDY OF LARGE-SCALE PROTO-TYPE TURBIDITY CURRENTS**

609 In this subsection, the present model was applied in a pilot study of the large-scale proto-type
610 turbidity currents in Xiaolangdi Reservoir, Yellow River in China. From 19th June to 13th July 2004,
611 water-sediment regulation experiment was conducted to make full use of the extra water storage to
612 reduce sedimentation in the Yellow River. During the whole experiment, two separate turbidity
613 current events were formed in the Xiaolangdi Reservoir by releasing sediment-laden flows from the
614 Sanmenxia and Wanjiazhai Reservoirs. Here the second event is revisited, as field data shows that the
615 first turbidity current dissipated at about 6.5 km upstream of the Xiaolangdi dam (Li 2004; YRCC
616 2007) and thus is unsuitable for whole-process modelling. The present pilot study covers the whole
617 process of the turbidity currents, from formation and propagation to recession, which is distinct from
618 work by Hu et al. (2012), which only modelled the propagation of turbidity currents while neglecting
619 the impacts of the clear-water flow in the upper layer.

620

621 **Case Description**

622 This turbidity current occurred in the afternoon of 7th July, about 1 day after the end of the first
623 event. Though indirectly, it was generated due to the water release from the Wanjiazhai Reservoir
624 between the 2nd and 7th July. When this water flow entered the Sanmenxia Reservoir and thus
625 increased its water storage, the flow discharge at Sanmenxia increased to approximately 5200 m^3/s,
626 which induced a second sediment-laden flood and thus the second turbidity current in the Xiaolangdi
627 Reservoir. There are 56 cross sections in the 130 km long main stream between Sanmenxia and
628 Xiaolangdi dams. And the impacts of tributaries in between the two dams are tentatively neglected as
629 they play a secondary role. The inflow discharge and its sediment concentration, which are actually
630 released from the Sanmenxia Reservoir, are shown in Fig. 10 along with the outflow discharge
631 through the Xiaolangdi dam. The inflow essentially relates to a hyperconcentrated flood modulated by
632 the Sanmenxia Reservoir. The time $t =$ 0 h corresponds to 13:00 7th July, when the flow discharge
633 at Sanmenxia reached its peak value. The computational time is 108 hours (from 13:00 7th July to
634 3:00 12th July). The total outflow discharge Q_{out}, comprised of a clear water discharge Q_w and
635 when appropriate a discharge Q_s of the turbidity current, was kept constant and amounted to 2700
636 m^3/s. A total of 18 bottom outlets with the depth of 5 m are distributed at different locations under the
637 dam. The maximum discharge for sediment flushing through the bottom outlets under the Xiaolangdi
638 dam was 1500 m^3/s. At the upstream boundary, the discharge was specified, and the velocity and depth
639 of the subaerial sediment-laden flow or clear-water flow were determined by the method of
640 characteristics. The downstream boundary conditions are implemented in a similar manner to those in
641 the subsection entitled *Sediment flushing efficiency*.

642 The initial bed topography is interpolated from 56 cross sections surveyed in May, 2004 (Fig. 11),
643 as the bed morphology immediately prior to the occurrence of the turbidity current was not surveyed.
644 Initially there is no turbidity current on the river bed. The following parameters are specified with
645 reference to the background of the Xiaolangdi Reservoir: $p =$ 0.4, $\rho_s =$ 2650 kg/m^3, and $d =$ 20
646 μm. Here the spatial step of 25 m is adopted. E_s is calculated through Eq. (13) following Hu et al.

(2012). The Courant number C_r is set to be 0.4. The interface roughness n_w adopted is set to be 0.005 $m^{-1/3}$ s, following the calibrated value for the test cases related to the laboratory experiments in the previous section. The bed roughness n_b and the correction coefficient α need to be calibrated by fitting to the measured front location. It is found that bed roughness n_b = 0.035 $m^{-1/3}$ s and correction coefficient α = 30 lead to satisfactory agreement with measured data. These calibrated parameters are appreciably different from those calibrated by Hu et al. (2012), which mostly can be ascribed to the limitation that the motion of the upper clear-water is not taken into account in the single layer-averaged by Hu et al. (2012).

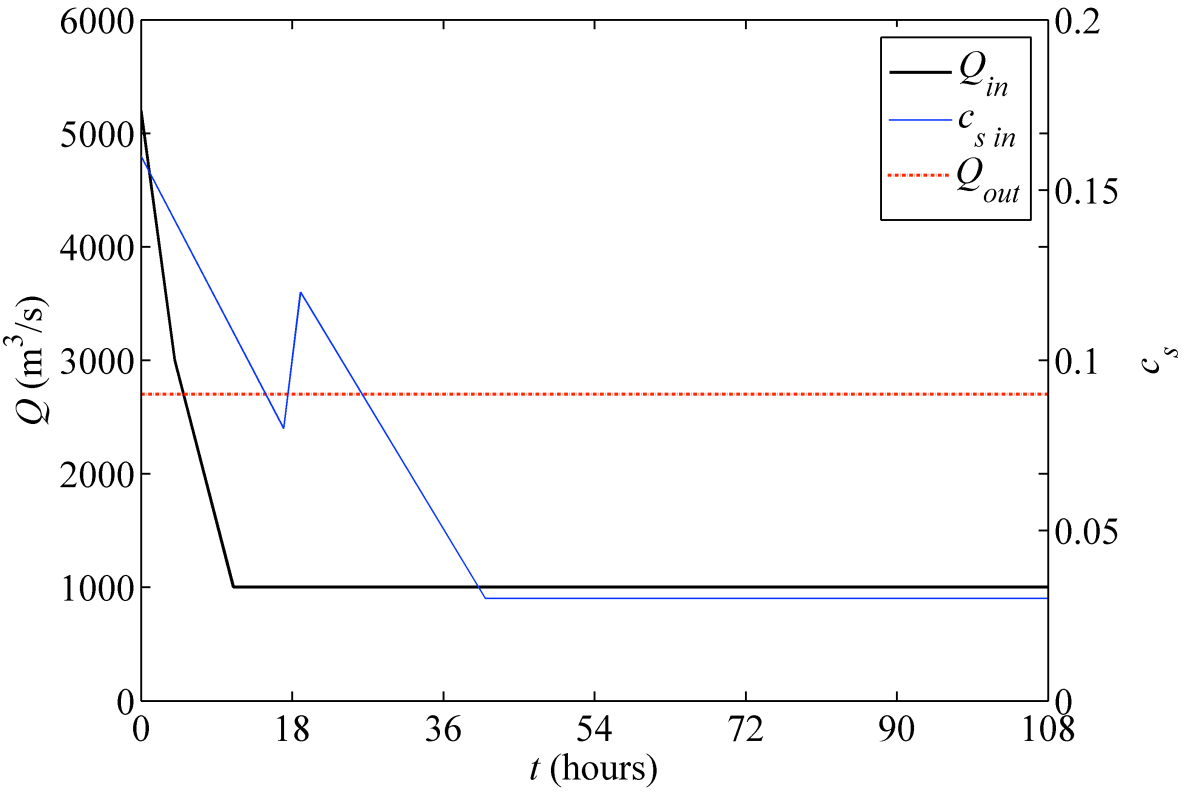

Fig. 10. Inflow discharge and sediment concentration along with outflow discharge

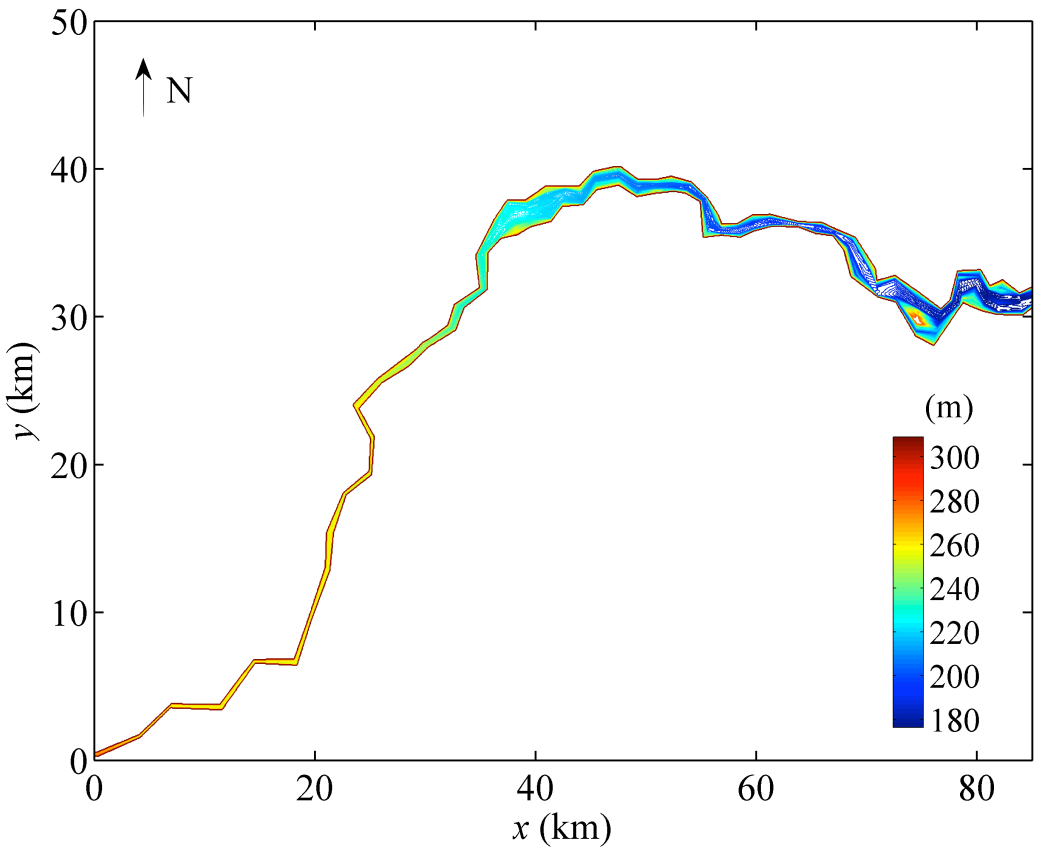

659

660 **Fig. 11.** Contour of initial bed topography based on the survey in May 2004

661

662 **Advance of Turbidity Currents**

663 Information on current advance can facilitate timely operation of the bottom outlets under the
664 dam so that sediment can be flushed out of the reservoir (Fan and Morris 1992a). If the bottom outlets
665 are closed upon the arrival of the current, the turbidity currents may lead to severe sedimentation, or
666 alternatively, if the bottom outlets are opened too early, stored water may be wasted. Shown in Fig. 12
667 is the computed front location of the sediment-laden flow (i.e., open-channel sediment-laden flow
668 upstream the plunging point or the turbidity current downstream the plunging), measured along the
669 course of the river. The measured data shown in Fig. 12 corresponds to the arrival time (approximately
670 $t =$ 20 h) of the turbidity current at Xiaolangdi dam. In Fig. 12, the computed results with the fine
671 grid (25 m) and a coarser grid (50 m) are included. The difference between the two mesh resolutions is
672 just marginally discernible, which demonstrates that the 25 m mesh resolution is sufficiently fine (i.e.,
673 mesh independence of the numerical solution is attained). From Fig. 12, the computed current

674 propagation with n_b = 0.035 and α = 30 compares best with the measured data. The advance of
675 the turbidity current front is mainly affected by the two parameters n_b and α. A faster advance is
676 generally obtained with a larger correction coefficient α and a smaller bed roughness n_b.
677 Physically, in relation to a larger correction coefficient α, bed sediment entrainment increases (Eq.
678 13), which leads to a higher sediment concentration and thus a larger driving force for the turbidity
679 current. Therefore it propagates faster. The larger the bed resistance, as represented by n_b, the more
680 energy the turbidity current dissipates and thus it propagates slower.

681

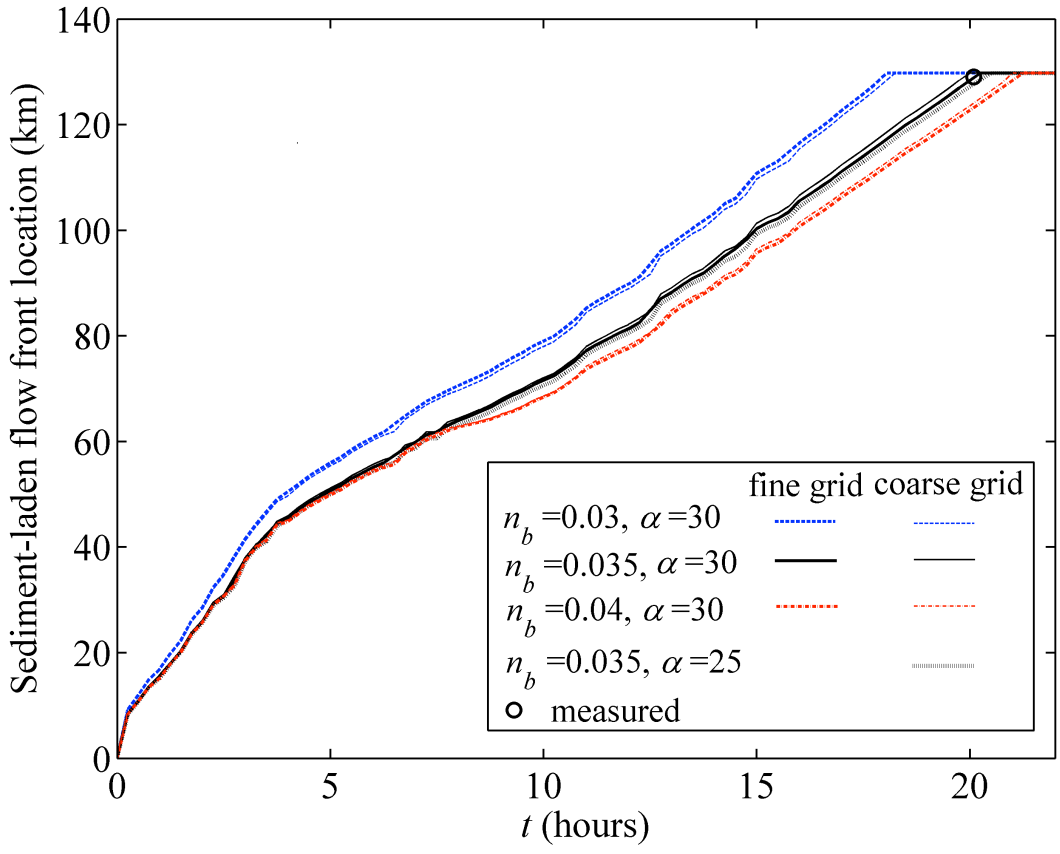

682

683 **Fig. 12.** Computed front location of sediment-laden flow compared with measured data

684

685 **Whole process of Turbidity Currents**

686 Figs. 13 and 14 demonstrate the formation, propagation and recession process of the turbidity

687 current by virtue of the clear-water layer thickness h_w, turbidity current thickness h_s and sediment
688 concentrations c_s respectively at four instants ($t =$ 4 h, 8 h, 20 h and 108 h). Also, Fig. 15 shows
689 the whole process of the turbidity current by means of the water surface, interface and bed along the
690 thalweg.

691 As illustrated in Figs. 13(a, b), 14(a) and 15(b), the flow at $t =$ 4 h is divided into two distinct
692 sections, i.e., the open-channel sediment-laden flow upstream and the clear-water flow downstream.
693 At about $t =$ 6.6 h, the open-channel sediment-laden flow advances to the cross section at
694 approximately $x =$ 38 km, characterized by an abrupt increase in longitudinal bed slope (Fig. 11).
695 Here the turbid water plunges into the clear water and begins to propagate as underflow, which marks
696 the formation of turbidity current. Alternatively, the plunge point is located at roughly 56.5 km from
697 the inlet along the course of the river, as shown in Fig. 15(c). From Fig. 14(b), a current with relatively
698 high sediment concentration is formed and the highest sediment concentration occurs at the front.

699 After traveling about 13.5 hours since its formation, the turbidity current arrives at the Xiaolangdi
700 dam [Fig. 12, Fig. 13(e, f), Fig. 14(c), Fig. 15(d)] and begins to be drained out through the bottom
701 outlets; the largest turbidity current thickness occurs at the narrowest cross section (at $x =$ 65 km and
702 $y =$ 35 km roughly); and the plunge point has hardly migrated downstream the plunging point at
703 $x =$ 38 km [Fig. 15(d)]. As shown in Fig. 14(c), the sediment concentration starts to reduce gradually
704 except in the section close to the inlet where sediment-laden flow continues to be released (Fig. 10).

705 After being vented through the bottom outlets for about 88 hours, the thickness of the turbidity
706 current [Fig. 13(h)] and sediment concentration [Fig. 14(d)] have decreased considerably, along with a
707 significant movement of the plunge point to the downstream [Fig. 15(f)]. In a way, this clearly reflects
708 a state of recession of the turbidity current. It is rational to anticipate that the turbidity current would
709 finally recede if clear water continues to be released at the Sanmenxia Reservoir and the turbidity
710 current is allowed to flush through the bottom sluice gates under the Xiaolangdi dam.

711 These observations along with the reasonable agreement with observed data for the turbidity
712 current advance suggest that the present model with properly specified parameters can properly
713 resolve the whole process of turbidity currents in Xiaolangdi Reservoir.

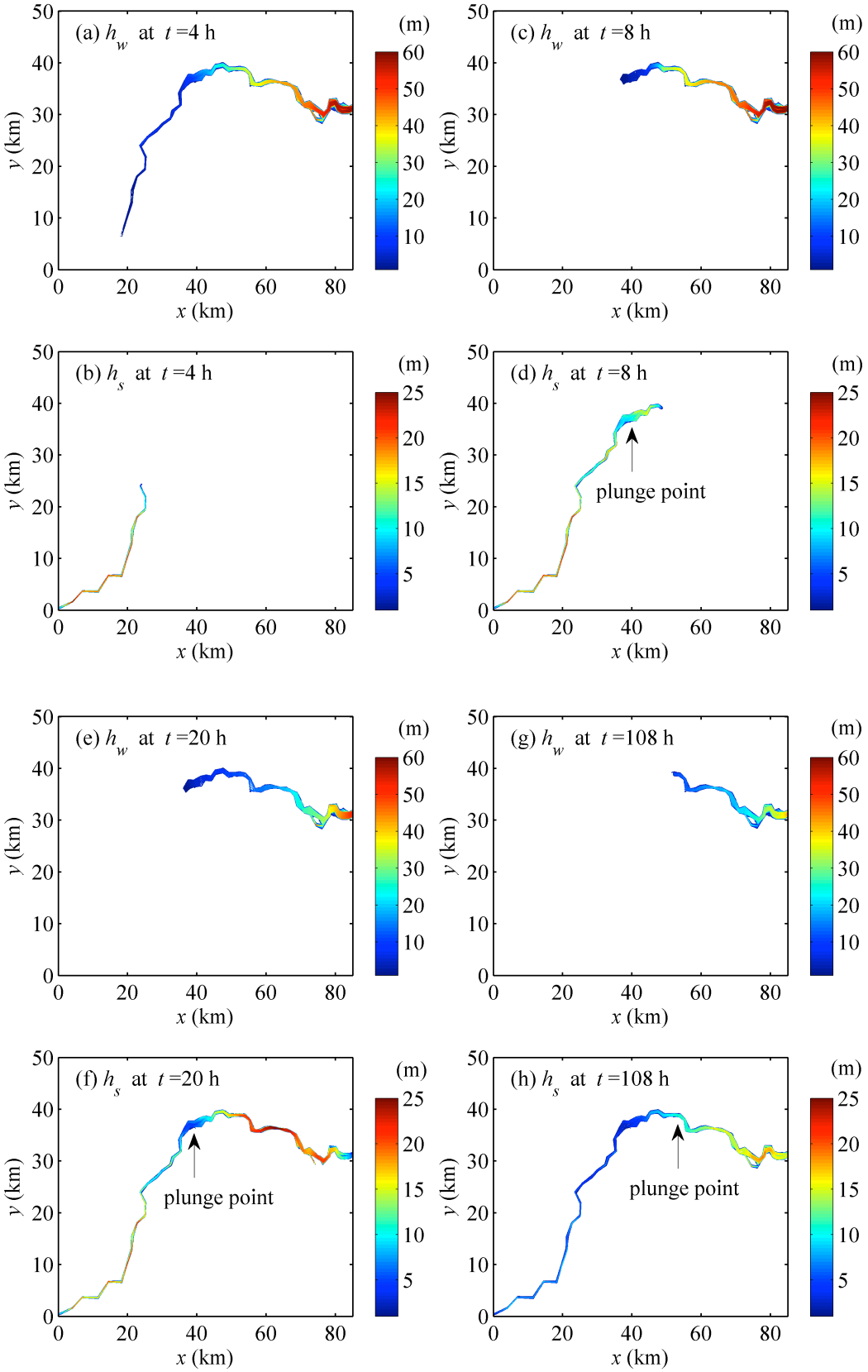

Fig. 13. Distributions of turbidity current thickness and clear-water thickness

718

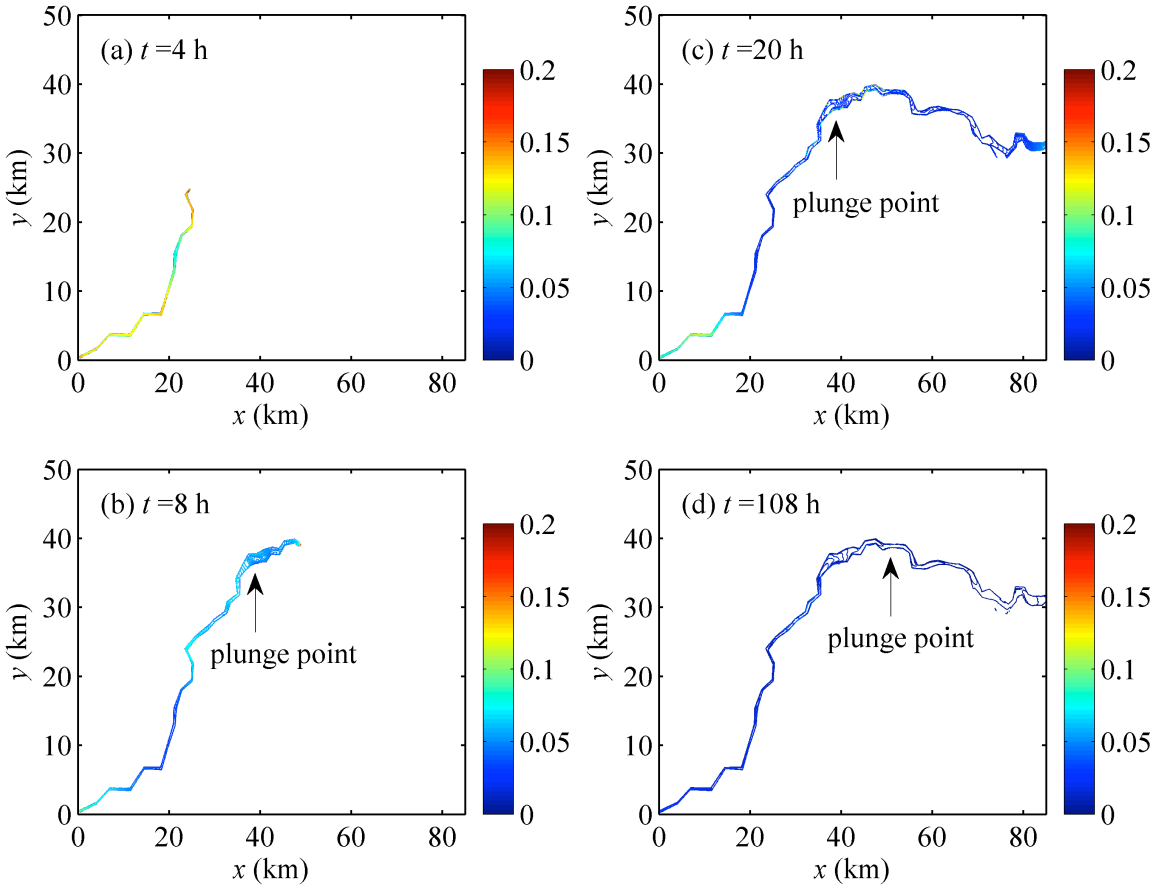

719

720 **Fig. 14.** Distributions of volumetric sediment concentration

721

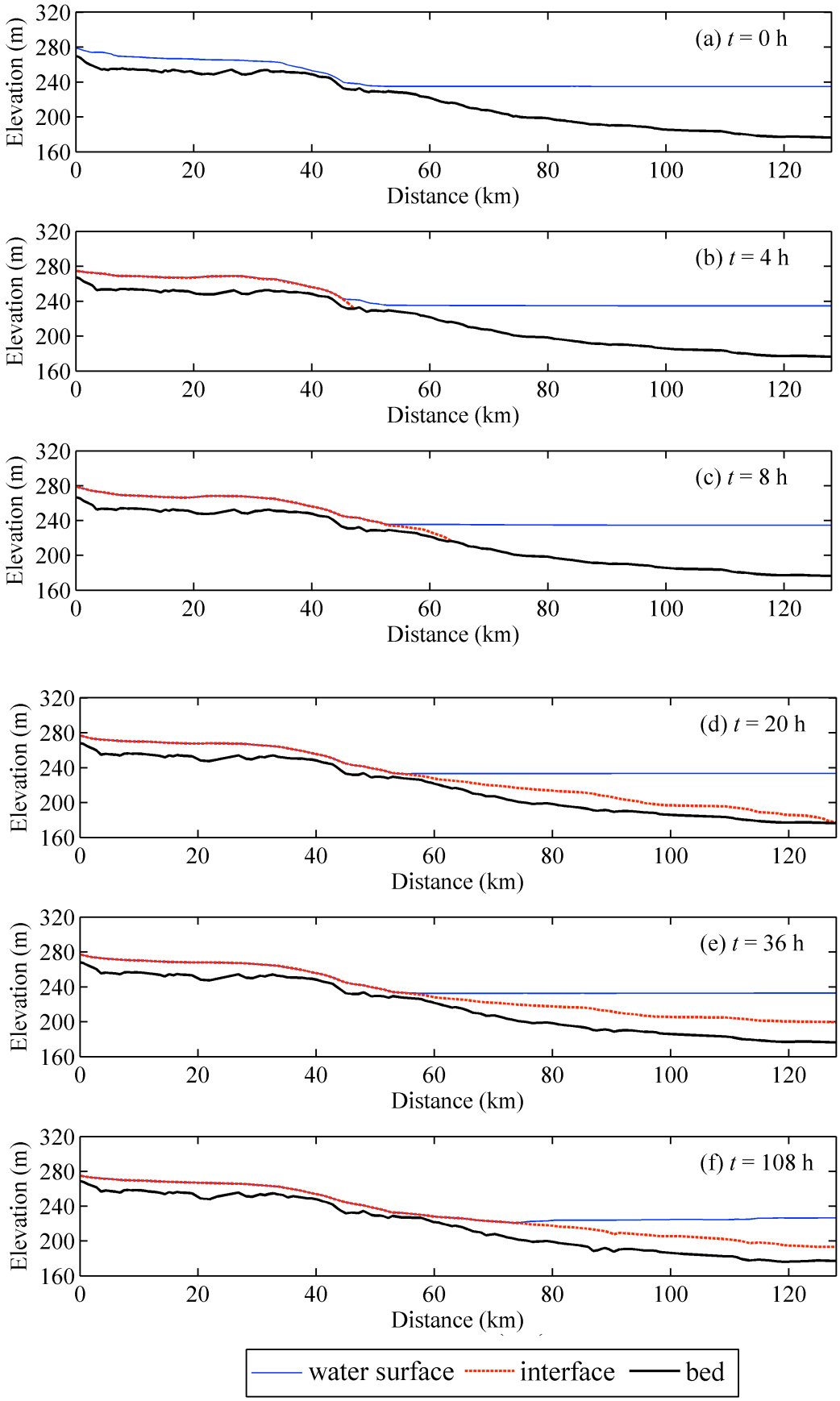

722

723

724 **Fig. 15.** Water surface, interface and bed profiles along the thalweg

725

726 **Bed Deformation and Sediment Mass Conservation**

727 Fig. 16 shows the bed scouring depth, defined as $z_b(x,y,0) - z_b(x,y,t)$. The turbidity current
728 appears to be erosive during the early stage, as indicated by the positive values of the bed scouring
729 depth [Fig. 16(a, b)]. This is a clear manifestation of the occurrence of bed scour. Physically, this is
730 attributable to the rather high discharge and sediment input released at the Sanmenxia Reservoir
731 combined with the discharge through the Xiaolangdi dam (Fig. 10). As the inflow discharge and
732 sediment concentration decrease gradually, bed aggradation occurs during the course of the turbidity
733 current propagation toward the dam [Fig. 16(c, d)]. By $t =$ 108 h, the whole domain of the
734 Xiaolangdi reservoir sees bed aggradation, except locally narrow reaches [Fig. 16(d)].

735 For turbidity currents in an ocean environment, it has been suggested that self-accelerating
736 mechanism exists (Parker et al. 1986). Specifically, the current entrains sediment from the bed, which
737 leads to a higher sediment concentration, and thus a larger difference in its density from the ambient
738 water. This essentially corresponds to an increase in the driving force for the current. Then, the current
739 accelerates, and picks up more sediment from the bed, which further accelerates the current. Therefore,
740 a self-reinforcing cycle is established. This mechanism cannot be precluded for the reservoir turbidity
741 current in question, as the influence of the coefficient α in relation to bed sediment entrainment [Eq.
742 (13)] is marginally detectable (Fig. 12). Nevertheless, it is hard to isolate the effect of the
743 self-accelerating mechanism from the control of the up- and downstream boundary conditions in the
744 reservoir. This is also the case for the effect of sediment deposition out from the turbidity currents,
745 which is opposite to the influence of the self-accelerating mechanism. Fortunately, all of those are
746 properly incorporated in the present fully coupled model.

747 An evaluation of the global sediment mass conservation is certainly warranted as it can reveal not
748 only the bulk aggradation or degradation in the Xiaolangdi Reservoir along with sediment flushing
749 efficiency, but the performance of the present model. It accounts for the budget of the sediment that
750 enters the Xiaolangdi Reservoir from the release at the Sanmenxia Reservoir, is flushed out at the
751 Xiaolangdi Reservoir by means of turbidity current, and also the sediment content within the flow. For
752 this purpose, the volume $V_{sc}(t)$ of the sediment contained within the flow is calculated by

$$V_{sc}(t) = \iint h_s c_s dxdy \tag{34}$$

and the volume of the sediment due to bed erosion or deposition by $V_{sb}(t)$,

$$V_{sb}(t) = (1-p)\iint [z_b(x,y,0) - z_b(x,y,t)]dxdy \tag{35}$$

The volume $V_{si}(t)$ of the sediment input from the upstream, and that $V_{so}(t)$ carried away through the bottom outlets are respectively,

$$V_{si}(t) = \iint (h_s u_s c_s)_{inlet} dydt, \qquad V_{so}(t) = \iint (h_s u_s c_s)_{outlet} dydt \tag{36a, b}$$

The bulk mass conservation of the sediment phase provides that the residual sediment volume

$$R_s \equiv V_{si}(t) - V_{so}(t) + V_{sb}(t) - V_{sc}(t) + V_{sc}(0) = 0 \tag{37}$$

In a perfect case, R_s should vanish, but in general it does not due to numerical errors. It is an important indicator of the performance of a numerical model in the sense of mass conservation. A positive value of $V_{sb}(t)$ means bulk degradation and the reverse demonstrates a bulk aggradation.

The volumes of sediment input from the upstream boundary (V_{si}), carried away through the bottom outlets (V_{so}), scoured from or deposited at the bed (V_{sb}), and contained within the flow (V_{sc}) along with their residuals (R_s) are illustrated in Fig. 17. It is demonstrated that by t = 18 h, there is no sediment flushed out from the reservoir (V_{so} = 0) as the turbidity current has not yet arrived at the bottom outlets. Before t = 18 h, the sediment volume contained within the flow (V_{sc}) exceeds the sediment input from upstream (V_{si}), thus the sediment scoured from bed is considerable (V_{sb} > 0), echoing the occurrence of bed scour as illustrated in Fig. 16(a, b). Along with the gradual reduction of the sediment input rate, both V_{sc} and V_{sb} decrease, and especially V_{sb} reduces to be negative, which means a shift from bulk degradation to bulk aggradation in the Xiaolangdi Reservoir. At approximately t = 20.5 h, due to the arrival of the turbidity current, the bottom sluicing gates under Xiaolangdi dam are opened for sediment flushing, inducing sediment output. After t = 60 h, the

775 sediment input rate becomes stable, V_{so} increases gradually, V_{sc} is little changed, while V_{sb}
776 decreases further, characterizing continuous bulk aggradation. At t = 108 h, about 1.173×10^7 (m^3) of
777 sediment has been flushed downstream by means of the turbidity current, while the bulk aggradation
778 in the Xiaolangdi Reservoir amounts to 1.196×10^7 (m^3), which are respectively equivalent to 37.47%
779 and 38.2% of the sediment input from the Sanmenxia Reservoir. The sediment flushing efficiency
780 (37.47%) of this particular turbidity current is consistent with the empirical range (18% - 36%) for the
781 Sanmenxia Reservoir (Fan and Morris 1992b) immediately upstream the Xiaolangdi Reservoir. Yet
782 this sediment flushing efficiency is considerably lower than others that can be over 60% (Fan and
783 Morris 1992b). Echoing the observations (Figs. 8 and 9) derived from the computational tests in
784 relation to the laboratory experiments by Lee and Yu (1997), further investigations are necessary to
785 optimize the reservoir operation scheme in line with differing inflow and sediment inputs so that the
786 sediment flushing efficiency can be maximized.

787 There has been no estimate of the bulk aggradation during the period of this particular turbidity
788 current to confirm the present modelling in this regard. Yet according to YRCC (2007), the bulk
789 aggradation was about 6.0×10^7 (m^3) over two months, during which two turbidity current events
790 occurred, and the first (from 18:00 5th to 19:00 6th July 2004) did not manage to reach the Xiaolangdi
791 dam and therefore the sediment released from the Sanmenxia Reservoir entirely deposited on the bed.
792 Given this information and also that tributary contributions have been neglected in the present
793 modelling, the amount of bulk aggradation (1.196×10^7 m^3) in connection with the particular turbidity
794 current studied herewith is reasonable. Equally notably, the bulk residual (R_s) of sediment in the
795 Xiaolangdi Reservoir is very small (Fig. 17), compared to the sediment volumes scoured from or
796 deposited at the bed, input from the upstream or output through the bottom outlets. More specifically,
797 the ratio of the residual R_s to V_{si} is only 1.61%. This further confirms the excellent performance of
798 the present model to resolve reservoir turbidity currents.

799

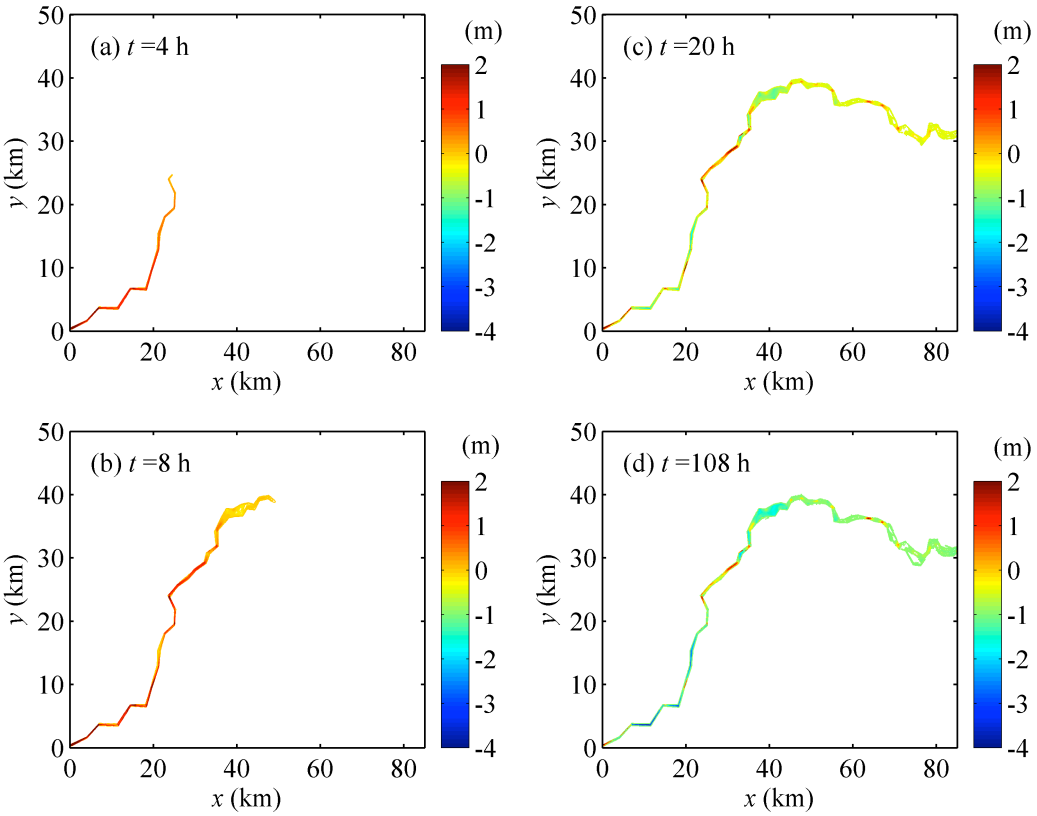

800
801 **Fig. 16.** Distributions of bed scouring depth

802

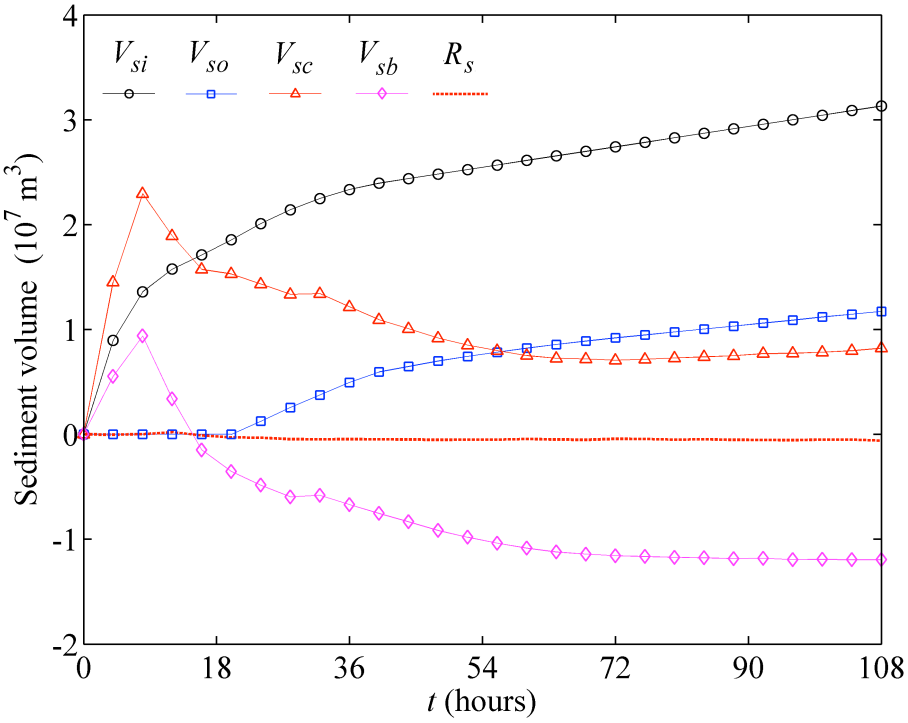

803
804 **Fig. 17.** Sediment volumes input from the upstream, output through bottom outlets, scoured from or
805 deposited at the bed, contained within the flow and their residuals

CONCLUSIONS AND REMARKS

A new 2D double layer-averaged model is developed, facilitating for the first time whole-process modelling of reservoir turbidity currents over erodible, irregular bed. Unsteady inflow discharge and sediment inputs as well as outflow hydrographs can be readily incorporated. It has been demonstrated to perform very well compared to a spectrum of laboratory experiments and rather satisfactorily in comparison with field data collected in the Xiaolangdi Reservoir, Yellow River in China. This work facilitates a viable and promising tool for the whole-process modelling of reservoir turbidity currents, in support of reservoir sediment management.

Computational tests using the present model reveal that an appropriate clear-water outflow is favourable for the propagation of turbidity currents, and also conducive to enhancing sediment flushing efficiency. This is significant for optimal operations of reservoirs suffering from sedimentation problems. However, it remains to be unraveled if an excessive clear-water outflow would spoil the turbidity currents that have already formed, as a result of Kelvin-Helmholtz instability. Further investigations are necessary to delimit quantitatively the impacts of reservoir operation schemes on sediment flushing by means of turbidity currents.

Uncertainty of the model mainly arises from the estimations of the interface and bed resistances as well as bed sediment entrainment, which certainly warrant systematic fundamental investigations of the mechanisms of turbidity currents. Uncertainty can be dealt with by empiricism that can be accrued through practice using more measured datasets. In its present form, the double layer-averaged model is confined to single sized sediment transport, whilst practically sediments in turbidity currents may be heterogeneous. Also, turbidity currents with high contents of fine sediments may behave as non-Newtonian fluids, which necessitate physically improved constitutive relationships to be incorporated in the model. These are reserved for future studies.

ACKNOWLEDGEMENTS

The research is funded by Natural Science Foundation of China (Grant Nos. 10932012 and 10972164).

834

835 **NOTATION**

836 *The following symbols are used in this paper:*

837 C_r Courant number (-)

838 c_b local near-bed concentration (-)

839 c_s volumetric sediment concentration of the turbidity current layer (-)

840 d medium sediment particle diameter (m)

841 **E** vector defined in Eq. (3)

842 E, D sediment entrainment and deposition fluxes respectively (m s^{-1})

843 E_s near-bed concentration at capacity condition

844 E_w mass exchange flux of clear water between the two layers (m s^{-1})

845 e_w coefficient for mass exchange of clear water (-)

846 **F** vector defined in Eq. (3)

847 F_p densimetric Froude number at plunge point (-)

848 **G** vector defined in Eq. (4)

849 g gravitational acceleration (m s^{-2})

850 g' submerged gravitational acceleration (m s^{-2})

851 **H** vector defined in Eq. (4)

852 h_p plunge depth (m)

853 h_s depth of turbidity current layer (m)

854 h_w depth of clear-water flow layer (m)

855 i, j spatial node indexes

856 k index denoting the time step

857 n_b bed roughness ($m^{-1/3}$ s)

858 n_w interface roughness ($m^{-1/3}$ s)

859 p bed sediment porosity (-)

860 q index denoting the auxiliary time step

861 q_{wx}, q_{wy} conservative variables in Eq. (3)

862 q_{sx}, q_{sy}, q_c conservative variables in Eq. (4)

863 $\mathbf{R}_b$, $\mathbf{R}_f$, $\mathbf{R}_e$ source terms for the clear-water flow layer

864 R_s residuals of sediment conservation (m^3)

865 r_b empirical coefficient (-)

866 Ri Richardson number (-)

867 s specific gravity of sediment (-)

868 $\mathbf{S}_b$, $\mathbf{S}_f$, $\mathbf{S}_e$ source terms for the turbidity current layer

869 $\mathbf{T}$ vector of conserved variables of the clear-water flow layer

870 t time (s)

871 $\mathbf{U}$ vector of conserved variables of the turbidity current layer

872 $\overline{U_s}$ resultant velocity of the turbidity current layer ($m\ s^{-1}$)

873 $\overline{U_{ws}}$ resultant velocity difference between two layers ($m\ s^{-1}$)

874 u_s, v_s mean velocities of the turbidity current layer in x - and y - directions ($m\ s^{-1}$)

875 u_w, v_w mean velocities of the clear-water flow layer in x - and y - directions ($m\ s^{-1}$)

876 u_*, v_* friction velocity in x - and y - directions ($m\ s^{-1}$)

877 $V_{si}(t)$, $V_{so}(t)$, $V_{sb}(t)$, $V_{sc}(t)$ sediment volumes input from the upstream, output through bottom

878 outlets, scoured from or deposited at the bed, contained within the flow, respectively (m^3)

879 x, y horizontal coordinates (m)

880 x_p distance between the plunge point and flume entrance (m)

881 z_b bed elevation (m)

882 α correction coefficient (-)

883 Δx, Δy spatial step in x - and y - directions (m)

884 Δt time step (s)

885 η water surface elevation (m)

886 η_s interface elevation (m)

887 v kinematic viscosity of water (m^2 s^{-1})

888 ρ_w, ρ_s densities of water and sediment, respectively (kg m^{-3})

889 ρ_c, ρ_0 densities of water-sediment mixture and saturated bed (kg m^{-3})

890 τ_{bx}, τ_{by} bed shear stress in x - and y - directions (kg m^{-1} s^{-2})

891 τ_{wx}, τ_{wy} interface shear stress in x - and y - directions (kg m^{-1} s^{-2})

892 ω settling velocity of a single sediment particle in tranquil clear water (m s^{-1}), and

893 ψ parameter in Eq. (12) (-)

894

895 **REFERENCES**

896 An, S., and Julien, P. (2014). "Three-dimensional modeling of turbid density currents in Imha
897 Reservoir, South Korea." *J. Hydraul. Eng.*, DOI: 10.1061/(ASCE)HY.1943-7900.0000851.

898 Adduce, C., Sciortino, G., and Proietti, S. (2012). "Gravity currents produced by lock exchanges:
899 experiments and simulations with a two-layer shallow-water model with entrainment." *J. Hydraul.*
900 *Eng.*, 138(2), 111-121.

901 Akiyama, J., and Stefan, H. G. (1984). "Plunging flow into a reservoir: Theory." *J. Hydraul. Eng.*,
902 110(4), 484-499.

903 Altinakar, M., Graf, W., and Hopfinger, E. (1996). "Flow structure of turbidity currents." *J.*
904 *Hydraul. Res.*, 34(5), 713-718.

905 Bradford, S. F., and Katopodes, N. D. (1999a). "Hydrodynamics of turbid underflows. I: Formulation
906 and numerical analysis." *J. Hydraul. Eng.*, 125(10), 1006-1015.

907 Bradford, S. F., and Katopodes, N. D. (1999b). "Hydrodynamics of turbid underflows. II: Aggradation,
908 avulsion, and channelization." *J. Hydraul. Eng.*, 125(10), 1016-1028.

909 Bonnecaze, R. T., Huppert, H. E., and Lister, J. R. (1993). "Particle-driven gravity currents." *J. Fluid*
910 *Mech.*, 250, 339-369.

911 Bonnecaze, R. T., Hallworth, M. A., Huppert, H. E., and Lister, J. R. (1995). "Axisymmetric
912 particle-driven gravity currents." *J. Fluid Mech.*, 294, 93-121.

913 Bournet, P. E., Dartus, D., Tassin, B., and Vincon-Leite, B. (1999). "Numerical investigation of

914 plunging density current." *J. Hydraul. Eng.*, 125(6), 584-594.

915 Cao, Z., Yue, Z. Y., and Pender, G. (2011). "Landslide dam failure and flood hydraulics. Part II:
916 coupled mathematical modelling." *Nat. Hazards*, 59, 1021-1045.

917 Chen, S. C., and Peng, S. H. (2006). "Two-dimensional numerical model of two-layer shallow water
918 equations for confluence simulation." *Adv. Water Res.*, 29(11), 1608-1617.

919 Choi, S. U. (1998). "Layer-averaged modelling of two-dimensional turbidity currents with a
920 dissipative-Galerkin finite element method. Part I: Formulation and application example." *J.*
921 *Hydraul. Res.*, 36(3), 339-362.

922 Castro, M., Frings, J., Noelle, S., Pares, C., and Puppo, G. (2010). "On the hyperbolicity of two- and
923 three-layer shallow water equations." *Proc., Int. Conf. Hyperbolic Problems,* Beijing, 657-664.

924 Dai, A., and Garcia, M. H. (2009). "Analysis of plunging phenomena." *J. Hydraul. Res.*, 47(5),
925 638-642.

926 Dallimore, C. J., Imberger, J., and Hodges, B. R. (2004). "Modeling a plunging underflow." *J.*
927 *Hydraul. Res.* 130(11), 1068-1076.

928 De Cesare, G., Schleiss, A., and Hermann, F. (2001). "Impact of turbidity currents on reservoir
929 sedimentation." *J. Hydraul. Eng.*, 127(1), 6-16.

930 Eggenhuisen, J. T., and McCaffrey, W. D. (2012). "The vertical turbulence structure of experimental
931 turbidity currents encountering basal obstructions: implications for vertical suspended sediment
932 distribution in non-equilibrium currents." *Sedimentology*, 59(3), 1101-1120.

933 Fan, J. (1960). "Experimental studies on density currents." *Scientia Sinica*, 9(2), 275-303.

934 Fan, J., and Morris, G. L. (1992a). "Reservoir sedimentation. I: Delta and density current deposits." *J.*
935 *Hydraul. Eng.*, 118(3), 354-369.

936 Fan, J., and Morris, G. L. (1992b). "Reservoir sedimentation. II: Reservoir desiltation and long-term
937 storage capacity." *J. Hydraul. Eng.*, 118(3), 370-384.

938 Fang, H. W., and Wang, G. Q. (2000). "Three-dimensional mathematical model of
939 suspended-sediment transport." *J. Hydraul. Eng.*, 126(8), 578-592.

940 Fukushima, Y., Parker, G., and Pantin, H. M. (1985). "Prediction of ignitive turbidity currents in
941 Scripps Submarine Canyon." *Mar. Geol.*, 67(1-2), 55-81.

942 Georgoulas, A. N., Angelidis, P. B., Panagiotidis, T. G., and Kotsovinos, N. E. (2010). "3D numerical
943 modelling of turbidity currents. Environ." *Fluid Mech.*, 10(6), 603-635.

944 Gladstone, C., Phillips, J. C., and Sparks, R. S. J. (1998). "Experiments on bidisperse,
945 constant-volume gravity currents: propagation and sediment deposition." *Sedimentology*, 45(5),
946 833-844

947 Guo, J. (2002). "Logarithmic matching and its application in computational hydraulics and sediment
948 transport." *J. Hydraul. Res.*, 40 (5), 555-565.

949 Hallworth, M. A., and Huppert, H. E. (1998). "Abrupt transitions in high-concentration,
950 particle-driven gravity currents." *Phys. Fluids*, 10(5), 1083-1087.

951 Hallworth, M., Huppert, H. E., and Ungarish, M. (2003). "On inwardly propagating
952 high-Reynolds-number axisymmetric gravity currents." *J. Fluid Mech.*, 494, 255-274.

953 Hirsch, C. (1990). *Computational methods for inviscid and viscous flows: Numerical computation of*
954 *internal and external flows.* Wiley, New York.

955 Huang, H., Imran, J., and Pirmez, C. (2007). "Numerical modeling of poorly sorted depositional
956 turbidity currents." *J. Geophys. Res.*, 112, 1-15.

957 Huang, H., Imran, J., and Pirmez, C. (2008). "Numerical study of turbidity currents with
958 sudden-release and sustained-inflow mechanisms." *J. Hydraul. Eng.*, 134(9), 1199-1209.

959 Hu, P., and Cao, Z. (2009). "Fully coupled mathematical modeling of turbidity currents over erodible
960 bed." *Adv. Water Resour.*, 32(1), 1-15.

961 Hu, P., Cao, Z., Pender, G., and Tan, G. (2012). "Numerical modelling of turbidity currents in the
962 Xiaolangdi reservoir, Yellow River, China." *J. Hydrol.*, 464, 41-53.

963 Hürzeler, B. E., Imberger, J., and Ivey, G. N. (1996). "Dynamics of turbidity current with reversing
964 buoyancy." *J. Hydraul. Eng.*, 122(5), 230-236.

965 Kassem, A., and Imran, J. (2001). "Simulation of turbid underflows generated by the plunging of a
966 river." *Geology*, 29(7), 655-658.

967 Kassem, A., Imran, J., and Khan, J. A. (2003). "Three-dimensional modeling of negatively buoyant
968 flow in diverging channels." *J. Hydraul. Eng.*, 129(12), 936-947.

969 Khan, S. M., Imran, J., Bradford, S., and Syvitski, J. (2005). "Numerical modeling of hyperpycnal
970 plume." *Mar. Geol.*, 222, 193-211.

971 Kim, J., and LeVeque, R. J. (2008). "Two-layer shallow water system and its applications." *Proc., Int.*
972 *Conf. Hyperbolic Problems*, Maryland, 737-743.

973 La Rocca, M., Adduce, C., Sciortino, G., Pinzon, A. B., and Boniforti, M. A. (2012). "A two-layer
974 shallow-water model for 3D gravity currents." *J. Hydraul. Res.*, 50(2), 208-217.

975 Lai, Y. G., and Wu, K. (2013). "Modeling of turbidity current and evaluation of diversion plans at
976 Shihmen Reservoir in Taiwan." *World Environment and Water Resources Congress 2013:*
977 *showcasing the future,* ASCE, 1736-1746.

978 Lee, H. Y., and Yu, W. S. (1997). "Experimental study of reservoir turbidity current." *J. Hydraul.*
979 *Eng.*, 123, 520-528.

980 Lee, W. K., Borthwick, A. G., and Taylor, P. H. (2014). "Tracer dynamics in two-layer
981 density-stratified estuarine flow." *Proc. Inst. Civil Eng.- Eng. and Comput. Mech.*, 167(1), 41-49.

982 Liang, Q. (2010). "Flood simulation using a well-balanced shallow flow model." *J. Hydraul. Eng.*,
983 136(9), 669-675.

Li, J., Cao, Z., Pender, G., and Liu, Q. (2013). "A double layer-averaged model for dam-break floods over erodible bed." *J. Hydraul. Res.*, 51(5), 518-534.

Li, G. Y. (2004). "The third test of water and sediment regulation conducted on the Yellow River." *Yellow River*, 26 (10), 1-8 (in Chinese).

Li, Y., Zhang, J., and Ma, H. (2011). "Analytical Froude number solution for reservoir density inflows." *J. Hydraul. Res.*, 49(5), 693-696.

Nourmohammadi, Z., Afshin, H., and Firoozabadi, B. (2011). "Experimental observation of the flow structure of turbidity currents." *J. Hydraul. Res.*, 49(2), 168-177.

Parker, G., Fukushima, Y., and Pantin, H. M. (1986). "Self-accelerating turbidity currents." *J. Fluid Mech.*, 171, 145-181.

Parker, G., and Toniolo, H. (2007). "Note on the analysis of plunging of density flows." *J. Hydraul. Eng.*, 133(6), 690-694.

Rottman, J. W., and Simpson, J. E. (1983). "Gravity currents produced by instantaneous releases of a heavy fluid in a rectangular channel." *J. Fluid Mech.*, 135, 95-110.

Savage, S. B., and Brimberg, J. (1975). "Analysis of plunging phenomena in water reservoirs." *J. Hydraul. Res.*, 13(2), 187-205.

Sequeiros, O. E., Cantero, M. I., and Garcia, M. H. (2009). "Sediment management by jets and turbidity currents with application to a reservoir for flood and pollution control in Chicago, Illinois." *J. Hydraul. Res.*, 47(3), 340-348.

Singh, B., and Shah, C. R. (1971). "Plunging phenomenon of density currents in reservoirs." *La Houille Blanche*, 26(1), 59-64.

Toro, E. F. (2001). *Shock-capturing methods for free-surface shallow flows.* John Wiley & Sons, Chichester.

Ungarish, M., and Zemach, T. (2005). "On the slumping of high Reynolds number gravity currents in two-dimensional and axisymmetric configurations." *European J. Mechanics B/Fluids.*, 24(1), 71-79.

Wu, W., Rodi, W., and Wenka, T. (2000). "3D numerical modeling of flow and sediment transport in open channels." *J. Hydraul. Eng.*, 126(1), 4-15.

Yellow River Conservancy Commission (YRCC). (2007). *The Third Test of Water and Sediment Regulation Conducted on the Yellow River.* Yellow River Conservancy Press, Zhengzhou, China (in Chinese).

Zhang, R., and Xie, J. (1993). *Sedimentation research in China- systematic selections.* China Water Power Press, Beijing, China (in Chinese).

Zech, Y., Soares-Frazão, S., Spinewine, B., and Grelle, N. (2008). "Dam-break induced sediment movement: Experimental approaches and numerical modelling." *J. Hydraulic Res.*, 46(2), 176-190.

List of figure captions

Fig. 1. Plan view sketch of experimental flume (adapted from Bonnecaze et al., 1995)

Fig. 2. Numerical solutions compared with measured data for 2D lock-exchange turbidity current: (a) front location, and (b) final deposition density

Fig. 3. Turbidity current formation and propagation (Series C - TC 15)

Fig. 4. Computed turbidity current thickness at plunge point compared with analytical formulations, with two dash lines representing the incipient and stable plunge points due to Lee and Yu (1997)

Fig. 5. Temporal variation of plunge point location

Fig. 6. Computed densimetric Froude number and turbidity current thickness at plunge point compared with measured data (Series B-PP4)

Fig. 7. Computed dimensionless turbidity current thickness, velocity and sediment concentration compared with measured data

Fig. 8. Impacts of downstream boundary conditions: (a) computed turbidity current thickness at plunge point compared with measured data, (b) computed plunge location, and (c) computed front location (Series B -PP 4)

Fig. 9. Sediment flushing efficiencies for extended cases

Fig. 10. Inflow discharge and sediment concentration along with outflow discharge

Fig. 11. Contour of initial bed topography based on the survey in May 2004

1052 **Fig. 12.** Computed front location of sediment-laden flow compared with measured data

1053

1054 **Fig. 13.** Distributions of turbidity current thickness and clear-water thickness

1055

1056 **Fig. 14.** Distributions of volumetric sediment concentration

1057

1058 **Fig. 15.** Water surface, interface and bed profiles along the thalweg

1059

1060 **Fig. 16.** Distributions of bed scouring depth

1061

1062 **Fig. 17.** Sediment volumes input from the upstream, output through bottom outlets, scoured from or
1063 deposited at the bed, contained within the flow and their residua
1064

1065 # List of tables

1066 **Table 1** Summary of inflow conditions for all revisited experimental runs

Run	Series B		Run	Series C	
	Inflow conditions			Inflow conditions	
	q_{in} (cm^2/s)	c_s (10^{-3})		q_{in} (cm^2/s)	c_s (10^{-3})
PP 1	23.5	3.71	TC 1	24.23	4.36
PP 2	42.25	3.71	TC 2	24.76	7.16
PP 3	70.56	2.51	TC 3	42.25	3.63
PP 4	85.10	2.00	TC 4	41.63	7.27
PP 5	86.74	3.86	TC 5	41.78	10.78
PP 6	100.21	3.27	TC 6	68.01	2.36
PP 7	86.01	5.61	TC 7	68.22	4.27
PP 8	99.64	4.98	TC 8	67.90	6.67
PP 9	101.20	6.60	TC 9	68.28	8.59
PP 10	134.46	4.85	TC 10	85.27	2.10
			TC 11	85.45	3.88
			TC 12	85.21	5.43
			TC 13	84.70	7.37
			TC 14	97.56	3.10
			TC 15	97.52	4.73
			TC 16	97.40	5.99
			TC 17	96.47	7.81
			TC 18	116.07	6.81

1067

1068

1069

1070 **Table 2** Parameters at incipient and stable plunge points (Series B)

RUN	Incipient				Stable			
	h_p (cm)		F_p		h_p (cm)		F_p	
	meas.	comp.	Li et al.	comp.	meas.	comp.	Dai & Garcia	comp.
PP 1	5.36	5.31	0.81	0.86	6.87	6.80	0.62	0.63
PP 2	7.40	7.37	0.96	0.97	9.28	9.39	0.65	0.62
PP 3	10.25	9.97	0.96	0.96	13.85	14.12	0.69	0.68
PP 4	12.56	12.48	1.02	1.03	17.15	17.25	0.64	0.64
PP 5	10.57	10.46	0.98	0.99	13.19	12.95	0.70	0.68
PP 6	13.54	13.63	0.95	0.97	16.32	16.40	0.72	0.69
PP 7	9.68	9.45	0.97	0.98	12.63	12.52	0.64	0.64
PP 8	12.84	12.43	0.97	0.99	14.37	14.60	0.66	0.67
PP 9	10.68	10.26	1.05	1.06	13.45	13.69	0.64	0.64
PP 10	12.68	12.38	0.94	1.03	18.09	17.95	0.68	0.67

1071

1072

1073

1074 **Table 3** Parameters at incipient and stable plunge points (Series C)

Run	Incipient		Stable					
	F_p		x_p		h_p		F_p	
	Li et al.	comp.	meas.	comp.	meas.	comp.	Dai & Garcia	comp.
TC 1	0.85	0.87	6.03	6.025	6.64	7.88	0.62	0.61
TC 2	0.89	0.90	5.52	5.50	5.62	6.43	0.64	0.63
TC 3	0.96	0.98	7.10	7.12	8.91	9.73	0.66	0.68
TC 4	0.95	0.94	6.29	6.31	7.17	7.94	0.65	0.67
TC 5	0.97	0.95	10.05	10.12	14.31	15.18	0.63	0.61
TC 6	0.99	0.96	10.05	10.12	14.31	15.18	0.63	0.61
TC 7	1.01	1.0	9.65	9.60	11.31	12.46	0.59	0.58
TC 8	0.98	0.99	8.05	8.03	10.53	11.13	0.65	0.62
TC 9	0.97	0.97	7.76	7.68	10.02	10.89	0.64	0.63
TC 10	0.99	0.96	11.24	11.26	17.04	17.85	0.66	0.65
TC 11	0.98	0.95	10.13	10.09	14.49	15.26	0.65	0.64
TC 12	1.02	1.03	9.46	9.56	12.97	13.69	0.64	0.66
TC 13	0.99	0.96	8.58	8.63	11.16	11.86	0.66	0.67
TC 14	0.98	0.97	10.96	10.98	16.51	17.20	0.67	0.65
TC 15	1.01	0.99	10.04	10.03	14.29	14.96	0.65	0.66
TC 16	0.99	0.98	9.55	9.68	13.18	14.29	0.67	0.64
TC 17	1.02	1.03	8.71	8.74	11.44	12.35	0.63	0.65
TC 18	0.99	0.96	9.68	9.78	9.68	10.03	0.67	0.65

1075

1076

1077